



Instability damping and amplification of compressible boundary layers via acoustic wall impedance

Lara De Broeck^{1,2} , Simon Görtz^{1,2} , Patrick Alter¹, João Hennings de Lara¹ and Martin Oberlack^{1,2} 

¹Chair of Fluid Dynamics, Technische Universität Darmstadt, Otto-Berndt-Str. 2, 64287 Darmstadt, Germany

²Centre for Computational Engineering, Technische Universität Darmstadt, Dolivostr. 15, 64293 Darmstadt, Germany

Corresponding author: Lara De Broeck, debroeck@fdy.tu-darmstadt.de

(Received 13 July 2024; revised 19 December 2024; accepted 13 January 2025)

We investigate the stability of a compressible boundary layer over an impedance wall for both constant impedances and a frequency-dependent porous wall model. For an exponential mean flow profile, the solution of the Pridmore-Brown equation, i.e. the linearised Euler equations for compressible shear flows, is expressed exactly in confluent Heun functions and, with the boundary condition of acoustic wall impedance, reduced to a single algebraic eigenvalue equation. This, in turn, is solved asymptotically and numerically and provides the complete inviscid eigenvalue spectrum without spurious modes. The key finding is that impedance walls not only have a desirable stabilising effect on inviscid disturbances, but also induce new instabilities. The type of the destabilised mode and therefore also the direction of propagation of the modes with maximum growth rate as well as the destabilised wavenumbers depend significantly on the porous wall properties, in particular on the porous wall layer thickness. For small porous layer thicknesses, the impedance-induced instability is observed as a second mode instability, where we find above a critical porosity growth rates exceeding those present in the rigid-wall case.

Key words: boundary layer stability, compressible boundary layers, supersonic flow

1. Introduction

To understand and control the laminar-to-turbulent transition of supersonic and hypersonic boundary-layer flows plays a pivotal role in the field of aeronautics and aerospace. Since the viscous drag in turbulent boundary layers is considerably higher than in laminar ones, the boundary-layer transition leads to significant losses in performance (Saric 1994; Malmuth *et al.* 1998; Fedorov *et al.* 2001). Further, the transition to turbulence causes a drastic increase in heat flux (Malmuth *et al.* 1998; Fedorov *et al.* 2001). This is especially crucial in the context of hypersonic vehicle design, as the higher thermal load in the case of an early transition requires stronger thermal protection systems, leading to additional vehicle weight at the expense of efficiency and maximum possible payload (Whitehead 1989). Therefore, comprehensive studies have focused on the transition of high-velocity boundary layers aiming to predict and delay this process in order to maintain the laminar flow state as long as possible. The results showed that the boundary-layer transition is a multifaceted mechanism that evolves in various paths depending on the mean flow parameters and external disturbances (Reshotko 1976, 1991, 2006; Morkovin 1994; Schneider 1999; Fedorov 2011, 2015).

In low-disturbance environments such as high-altitude flights and for negligible surface roughness, boundary-layer transition results from the excitation of unstable modes (Morkovin 1994; Malik *et al.* 1990; Reshotko 1994). Small environmental disturbances enter the boundary layer and amplify the unstable modes in the flow through a receptivity process (Mack 1984; Fedorov 2015). In response, the unstable boundary-layer modes start to grow following the linear stability theory before nonlinear effects dominate and lead to the transition to turbulence (Mack 1969; Morkovin 1994; Fedorov 2015). Therefore, linear stability analyses, along with experiments, are crucial tools to predict the initial phase of transition and to develop measures to control the unstable linear growth in this phase in order to delay the transition process (Mack 1984; Malik 1989).

Important fundamental findings on linear boundary-layer stability were provided by the theoretical work of Lees & Lin (1946), who developed an inviscid stability theory for compressible boundary layers based on asymptotic analysis. Building on their pioneering work, numerous further numerical and experimental studies have been conducted to investigate the stability of supersonic and hypersonic boundary-layer flows. A seminal contribution to compressible boundary layer linear stability theory was provided by the extensive numerical investigations of Mack (1969, 1984). With his calculations Mack confirmed the results of Dunn & Lin (1955) and Lees & Reshotko (1962) that in boundary layers at moderate supersonic Mach numbers an instability mode occurs, the so-called first mode, which can be regarded as an extension to high velocities of the incompressible Tollmien–Schlichting waves (Mack 1984). It represents a viscous instability at low Mach numbers. However, as the Mach number increases, the inviscid character of the first mode becomes dominant (Mack 1984).

For boundary layers at higher Mach number, Mack (1963, 1964) found that many further unstable modes occur additionally to the first mode. These higher modes, also referred to as Mack modes, are high-frequency acoustic waves that reflect inviscidly between the wall and the sonic line (Mack 1969, 1987). They occur in boundary layers with insulated walls for Mach numbers greater than 2.2 (Malmuth *et al.* 1998). Among these higher modes, the mode with the lowest frequency, the so-called second mode, is of particular interest as it is the least stable of the higher modes (Mack 1984; Reed *et al.* 1996; Malmuth *et al.* 1998). For Mach numbers greater than about 4, the second mode becomes the dominant instability in the boundary layer growing faster than the first-mode disturbances. In the case of cooled walls, even for smaller Mach numbers, the second mode can become

dominant (Lysenko & Maslov 1984; Malik 1989). While for the first modes the oblique three-dimensional (3-D) disturbances prove to be considerably more unstable than the corresponding two-dimensional (2-D) ones, the reverse is true for the second and higher modes where 2-D disturbances are the most unstable (Mack 1984). The existence of the second-mode instabilities has already been shown in the experimental studies of Kendall (1975) and Demetriades (1974).

Due to the different character of the first mode and the higher acoustic modes, they respond differently to certain influencing factors and control measures. Whereas the first mode is damped by wall cooling (Lees & Lin 1946), which occurs naturally in hypersonic vehicles having wall temperatures even less than 0.2 of the adiabatic wall temperature, wall cooling on the other hand leads to destabilisation of the second and higher modes (Mack 1969, 1984). Therefore, the search for effective methods to suppress the second-mode instability is of great relevance for high-Mach-number boundary-layer-transition control. In this context, Kimmel (2003) makes a distinction between (a) passive control techniques such as local shaping (Malik 1989; Fedorov *et al.* 2001; Rasheed *et al.* 2002) and acoustic metasurfaces and (b) active techniques involving blowing and suction (Malik 1989) or CO₂ injection (Leyva *et al.* 2009; Fedorov *et al.* 2014).

One of the most promising transition control techniques are the so-called acoustic metasurfaces, such as porous coatings, as they barely affect the mean flow (Fedorov *et al.* 2003; Tian & Wen 2021). Also, porous coatings were found to be compatible with the thermal protection system surfaces of hypersonic vehicles, making them suitable as a transition delay measure for this application (Fedorov *et al.* 2003; Wagner *et al.* 2013, 2015). Applying passive porous linings was suggested by Malmuth *et al.* (1998), who assumed that porous surfaces can cause absorption of the perturbation energy of high-frequency acoustic disturbances and thus lead to stabilisation of the second and higher modes. This presumed effect, that porous walls, also known as ultrasonically absorptive coatings, can achieve a significant second-mode stabilisation, was later validated both experimentally and numerically (Malmuth *et al.* 1998; Fedorov *et al.* 2001, 2003, 2006; Rasheed *et al.* 2002; Wagner *et al.* 2013). This finding motivated further studies of the effect of ultrasonically absorptive coatings on hypersonic boundary-layer stability.

A recent study by Tian & Wen (2021) revealed that in addition to the energy absorption mechanism, a phase shift of the wall-normal energy transport is responsible for the stabilisation effect. As a result of the porous coating, the phase of the energy transport by the wall-normal velocity fluctuations is delayed relative to the phase of the internal energy fluctuation in the vicinity of the critical layer. This affects the interaction between the wall-normal fluctuations and the critical-layer fluctuations, resulting in a reduction in the second-mode growth rate.

In contrast to the stabilising effect on the second mode, the first mode is slightly destabilised by the presence of porous walls (Fedorov *et al.* 2003). The extent of the destabilisation of the first mode and the stabilising effects on the higher modes, though, depend strongly on the design of the porous walls, such as the pore depth (see e.g. Wartemann *et al.* 2009), the layer thickness or the wall material, but also on the wall temperature, for example. This motivated Brès *et al.* (2010), Tian *et al.* (2019) and Tian *et al.* (2022), among others, to investigate design strategies for porous layers to improve the second-mode control performance while reducing the first-mode destabilisation.

The destabilising effect of acoustic metasurfaces of impedance type was first postulated in the inviscid case by Rienstra (2003), who observed the occurrence of instabilities induced by impedance walls. In his work analysing an inviscid duct flow with wall linings of constant wall impedance Z , he observed so-called surface waves, which are mainly 2-D and which decay exponentially from the wall, making them relevant only near the

wall. Depending on the Mach number M and the impedance Z , different numbers of surface waves occur, up to a maximum of four, which can be divided into acoustic and hydrodynamic surface modes. By tracing the modes under variation of the wall impedance, Rienstra could show in the incompressible limit that at least for certain impedances one of the hydrodynamic surface waves becomes an instability. Rienstra's results on surface modes over impedance walls were confirmed and extended by Brambley (2013) taking into account the effects of a thin sheared boundary layer in the duct. To this end, he solves the inviscid governing equation for the pressure for a tanh and a linear boundary-layer profile by applying both numerical integration at Mach number $M = 0.5$ and other approximate methods, among others thin-boundary-layer asymptotics. For the acoustic surface impedance Z , a Helmholtz resonator model or a mass–spring–damper model are mainly applied. In his work, Brambley considers both temporal and convective instabilities. He finds that, compared with the maximum of four surface waves in the case of a uniform flow, there are at most six surface modes over the impedance wall for the sheared boundary layer, of which at least one is a convective instability. The occurrence of a hydrodynamic instability over a wall lining was confirmed experimentally by Aurégan & Leroux (2008) for a channel flow up to Mach 0.3. In addition, the experimental work by Marx *et al.* (2010) on a channel flow at Mach 0.27 shows that the interaction of flow and sound can also induce instability over a wall liner, which they claim can be a first- or second-mode instability.

Besides the classic concept of porous wall linings, other acoustic metasurface types have been developed in recent years to control the Mack second-mode instability, such as the impedance-near-zero metasurfaces proposed by Zhao *et al.* (2019) or so-called reflection-controlled acoustic metasurfaces (Zhao *et al.* 2021). A review of the research progress on the effects of different metasurfaces on the linear stability of high-velocity boundary layers was recently provided by Zhao *et al.* (2022).

Also against the background of decades of research, the stability behaviour of boundary-layer flows with acoustic surfaces is not yet fully understood. For example, the first-mode destabilisation induced by porous walls was found for viscous flows in the supersonic case. On the other hand, the works of Rienstra (2003) and Brambley (2013), showing the occurrence of unstable modes over impedance walls for the inviscid case, are limited to $M < 1$ and do not consider impedance models of the porous type. In this paper we therefore want to extend the investigations for the inviscid case to the practically relevant problem of supersonic boundary layers with a porous wall coating. The aim is to find out whether the same stabilisation and destabilisation effects as in the viscous studies are observed and whether any further effects occur. So we want to investigate whether, in addition to a second-mode stabilisation, a first-mode destabilisation by the porous wall also occurs in the inviscid case and whether beyond that destabilisation in the form of other unstable modes is also possible. Furthermore, the question arises as to how the most unstable mode occurring in the porous wall boundary layers and thus the direction of propagation of the strongest growth change under the porous wall. In the context of metasurface design, it is also of interest to explore whether destabilisation only happens with specific wall parameter configurations, and whether certain configurations can cause unstable growth rates greater than in the rigid-wall case. Motivated by these research gaps, we have derived in this work an exact solution for the inviscid linear boundary-layer stability problem, which allows us to study the aforementioned fundamental effects of acoustic metasurfaces comprehensively for a broad frequency range.

The mathematical basis for our investigations is the Pridmore-Brown equation (PBE), an ordinary differential equation for the linear perturbations in 2-D parallel shear flows, which was first derived by Pridmore-Brown (1958) from the linearised compressible Euler

equations by employing a normal mode ansatz for the perturbations. Thus, for a specific shear-flow profile inserted into the PBE, the PBE describes both stability and acoustic properties of the linear inviscid perturbations in the respective shear flow. In view of the great physical relevance of the PBE, different authors have already dealt with the search for solutions to the PBE. However, due to the mathematical complexity of this equation, analytical solutions could so far only be found for rare simple shear profiles. For the simplest case of a linear velocity profile to model a boundary-layer flow, Goldstein & Rice (1973) were the first to derive an exact solution of the PBE in terms of combined parabolic cylindrical functions. Due to the complex form of cylindrical functions of different orders, however, this solution has been little applied.

In a later study, Campos & Serrão (1998) considered an exponential velocity profile as a more physical model for the boundary layer. For the PBE with the exponential profile, they formulated a Frobenius–Fuchs series solution. However, since the PBE in this case has more than one regular singularity and also irregular singularities, the convergence radius of the solution is limited to the region between two singularities, implying that the entire domain cannot be described by one series solution, but requires connections between different regions of solutions. For this reason, Campos & Serrão (1998) mainly investigated the sound propagation in the boundary layer, thereby confirming the absorption of sound by the critical layer. However, they did not examine the boundary-layer stability. This prompted Zhang & Oberlack (2021) to search for a new exact solution to the PBE with exponential velocity profile, which allows both the acoustics and the stability of the boundary-layer flow to be investigated. They succeeded in deriving an exact solution in terms of the confluent Heun function (CHF). Using this solution, they were able to reduce the stability problem of boundary layers with rigid walls to an algebraic eigenvalue equation. Based on this eigenvalue equation, Zhang & Oberlack (2021) studied the temporal stability modes for a wide wavenumber spectrum and different Mach numbers.

Compared with the study of Zhang & Oberlack (2021), who considered the linear stability of boundary layers with rigid walls, we now want to extend the problem to boundary layers with acoustic metasurfaces. Similar to their work, our investigations are based on the PBE with an exponential mean velocity profile for the boundary-layer flow. To model the effect of the acoustic surface on the flow perturbations, we employ the acoustic impedance boundary condition (BC) $\hat{v}_w = \hat{p}_w/Z$ (Malmuth *et al.* 1998). This surface impedance BC is a common treatment in the context of linear stability theory analysis for boundary layers with metasurfaces (Fedorov *et al.* 2001). It links the normal-mode amplitudes of the vertical velocity perturbation v'_w and the pressure perturbation p'_w at the wall. The complex acoustic surface impedance Z depends on the wall properties such as its material and the microstructure geometry (including pore depth or diameter in the case of porous walls) as well as on mean flow characteristics at the wall and the disturbance wavenumber and frequency (Fedorov *et al.* 2001).

Based on the PBE with the exponential boundary-layer profile together with the far-field BC of vanishing perturbations and the surface impedance condition, we comprehensively investigate the fundamental effects of acoustic metasurfaces on the inviscid linear stability behaviour of compressible boundary layers using both numerical and theoretical methods.

This paper is structured as follows. First, in § 2, the basic model equations are introduced, i.e. the PBE along with the BCs, forming the eigenvalue problem of the boundary-layer stability problem. By using the exact solution of the PBE with exponential profile, we convert the eigenvalue problem to an algebraic equation. In § 3, based on the PBE and the BCs, the growth of 2-D and 3-D temporal instability modes is compared. Unlike for the boundary-layer problem with metasurfaces, there exists a transformation

between the 2-D and the 3-D modes for the rigid-wall problem, allowing us to derive a condition for dominance of the 2-D instabilities. In §4, we focus on the occurrence of new inviscid instability modes induced by the surface impedance. To this end, we perform an asymptotic analysis for small wavenumbers based on the algebraic eigenvalue equation to examine the branching behaviour of the solutions as a function of the surface impedance. Finally, in §5, we solve the eigenvalue equation numerically for the complex eigenvalues ω of the temporal stability case over a wide wavenumber range, examining different impedance values. Here we consider both constant real wall impedances for validating the asymptotic results as well as a porous wall impedance model. A decisive advantage in this context is that, owing to the exact PBE solution in terms of the CHF, we only obtain physical eigenvalues when solving the eigenvalue equation numerically, without the occurrence of spurious modes.

2. Basic model equations

This section presents the basic model equations that are used to describe the inviscid linear stability behaviour of compressible boundary-layer flow with wall coating. The PBE according to Pridmore-Brown (1958) and the BCs are derived, which together form the eigenvalue problem. The inviscid linear stability analysis is based on solving the linearised compressible Euler equations, which thus form the starting point for the derivation of the PBE. The inviscid theory was already used by Lees & Lin (1946) and Mack (1969, 1984) as a suitable method to study the linear stability of compressible boundary layers, owing to the inviscid character of the dominant instabilities in high-Mach-number boundary layers.

2.1. Pridmore-Brown equation

To derive the underlying inviscid linear stability equation, the PBE, we start with the compressible Euler equations, neglecting viscosity and heat conduction (Spurk & Aksel 2019). Accordingly, the model problem considered in this work is intended to shed light on the inviscid acoustic perturbations in the high-Reynolds-number limit (Rienstra & Hirschberg 2001; Delfs 2016). These assumptions hold especially for the high-frequency limit, as shown by Aurégan *et al.* (2001) and Brambley (2011), which analyse the effects of dissipation and shear on the BC at the wall.

The equations are linearised around a mean state, indexed by 0, giving the linearised Euler equations:

$$\frac{\partial \rho'}{\partial t} + \mathbf{v}_0 \cdot \nabla \rho' + \rho_0 \nabla \cdot \mathbf{v}' + \mathbf{v}' \cdot \nabla \rho_0 + \rho' \nabla \cdot \mathbf{v}_0 = 0, \quad (2.1a)$$

$$\rho_0 \left(\frac{\partial \mathbf{v}'}{\partial t} + \mathbf{v}_0 \cdot \nabla \mathbf{v}' \right) + \nabla p' + \rho_0 \mathbf{v}' \cdot \nabla \mathbf{v}_0 + \rho' \mathbf{v}_0 \cdot \nabla \mathbf{v}_0 = 0, \quad (2.1b)$$

$$p' = c^2 \rho', \quad (2.1c)$$

where \mathbf{v} denotes the velocity vector, ρ the density and p the pressure. The small unsteady perturbations are denoted by a prime. Equation (2.1c) represents the linearised thermodynamic equation of state $p = p(\rho, s)$ under the assumption of constant entropy, with $c = \sqrt{(\partial p / \partial \rho)_s}$ describing the speed of sound.

For the boundary-layer flow, we assume a parallel mean flow of the form $\mathbf{v}_0 = U_0(y) \cdot \mathbf{e}_x$, where y describes the wall-normal direction. In addition, we assume the mean flow as isothermal, implying a constant mean density ρ_0 .

It is noted that the isothermal assumption is a simplification, especially for the considered Mach number range, as thermal effects will influence the results quantitatively.

Eigenmodes are particularly influenced by the character and position of the critical layer, which exists for both an isothermal and a non-isothermal boundary layer. Since the position of the critical layer is slightly moved by a non-constant mean temperature profile, a quantitative modification of the isothermal results shown in this paper is to be expected. However, the qualitative observations made in this work will also be retained in the non-isothermal case. The aim of this work is therefore to reveal fundamental effects employing a model problem.

The resulting linearised Euler equations for the parallel shear flow are non-dimensionalised using ρ_0 , the far-field velocity U_∞ and the boundary-layer thickness δ . Due to homogeneity of the equations with regard to x , z and t , a normal-mode approach is applied, which for 2-D perturbations reads

$$q'(x, y, t) = \hat{q}(y)e^{i(\alpha x - \omega t)} \quad \text{with } q \in \{u, v, \rho\}. \quad (2.2)$$

While in this section only 2-D disturbances are considered, the explicit z dependence of disturbances through the wavenumber β is also taken into account in § 3. In the approach (2.2), $\hat{q}(y)$ denotes the complex amplitudes of the perturbations. For temporal stability analysis, we assume $\omega \in \mathbb{C}$ with its real part ω_r representing the temporal frequency and its imaginary part ω_i the temporal growth rate. Parameter $\alpha \in \mathbb{R}$ is the non-dimensionalised streamwise wavenumber. Applying (2.2) to the non-dimensionalised linearised Euler equations yields a coupled system of first-order ordinary differential equations (ODEs) for the perturbation amplitudes, which can be converted to a single ODE of second order for the density perturbation amplitude $\hat{\rho}(y)$:

$$\frac{d^2 \hat{\rho}}{dy^2} + \frac{2\alpha}{\omega - U_0\alpha} \frac{dU_0}{dy} \frac{d\hat{\rho}}{dy} + \left[M^2(\omega - U_0\alpha)^2 - \alpha^2 \right] \hat{\rho} = 0, \quad (2.3)$$

which is the so-called PBE. Here $M = U_\infty/c$ is the free-stream Mach number. The relations for the remaining perturbation amplitudes in terms of $\hat{\rho}(y)$ are given in Appendix A.

2.2. Boundary conditions

The eigenvalue problem is given by finding those values (α, ω) that ensure compatibility of the solution of the PBE (2.3) with the BCs of the problem. Since we aim to investigate instabilities originating from the boundary layer itself, we do not allow energy transfer from the far field to the inside of the boundary layer. Furthermore, an infinite perturbation amplitude in the far field would seem unphysical. This leads to the BC of bounded perturbation amplitude in the far field ($y \rightarrow \infty$) (Mack 1984). Also common in stability analysis is the more restrictive requirement for the amplitudes to vanish in the far field, giving

$$\lim_{y \rightarrow \infty} \hat{\rho}(y) = 0. \quad (2.4)$$

We will see later in this section that for the temporal stability problem with $\omega_i \neq 0$ the condition of bounded far-field amplitudes reduces to (2.4) for the model equations in this paper, which means that both far-field BCs yield the same stability eigenvalues.

While we use the BC (2.4) here, it should be noted that other literature advocates a different BC. Brazier-Smith & Scott (1984), Huerre & Monkewitz (1985), Crighton (1989), Riedinger *et al.* (2010) and Brambley & Gabard (2014), among others, apply causality arguments that lead to unbounded behaviour in the far field. Riedinger *et al.* (2010, p. 258) comment in particular that ‘The difficulty with this condition is that it does not necessarily imply that the solution vanishes at infinity when the modes are neutral or damped ($\text{Im } \omega <$

0)’, while Brambley & Gabard (2014, p. 5562) find ‘leaky surface waves excited by a line source that grow exponentially away from the surface’. However, for temporal instabilities with $\text{Im } \omega > 0$, there is a consensus that the behaviour at infinity should be bounded, in agreement with (2.4). Thus, the results presented in the following of this paper could be easily modified to use alternative BCs instead of (2.4).

The second BC for $\hat{\rho}$ is set up on the wall ($y = 0$). Since we consider an acoustic metasurface, we apply the acoustic impedance BC, which in the case of a straight wall without mean flow along the wall reads (Malmuth *et al.* 1998; Rienstra & Darau 2011)

$$\hat{\rho} = -Z \hat{v} \quad \text{for } y = 0. \tag{2.5}$$

Equation (2.5) links the wall-normal velocity perturbation and the pressure perturbation at the wall via the complex surface impedance Z , which depends on the wall and mean flow properties, such as the Mach number, as well as the perturbation frequency and wavenumber (Malmuth *et al.* 1998; Zhao *et al.* 2022). Consequently, (2.5) describes the effect of the surface on the boundary-layer stability. The limit $Z \rightarrow \infty$ describes a rigid wall (Campos & Serrão 1998). In order to express (2.5) in terms of the density perturbation $\hat{\rho}$, we substitute \hat{v} by (A2) and \hat{p} by $\hat{p} = (1/M^2)\hat{\rho}$ resulting from (2.1c) by non-dimensionalising, which yields

$$\left. \frac{d\hat{\rho}}{dy} \right|_{y=0} = -i\omega Y \hat{\rho}(0) \tag{2.6}$$

with $Y = Z^{-1}$ denoting the acoustic admittance and thus $Y = 0$ representing the rigid-wall case. The two BCs (2.4) and (2.6) together with the PBE (2.3) form the eigenvalue problem for (α, ω) , which we solve for $\alpha \in \mathbb{R}$ and $\omega \in \mathbb{C}$.

Using symmetry considerations given in Appendix B, it can be shown that in the case of rigid walls $Y = 0$, the eigenvalues (α, ω) occur both complexly conjugated and reflected, meaning that, together with an eigenvalue (α, ω) , also (α, ω^*) and $(-\alpha, -\omega)$ occur as further solutions, having the opposite stability behaviour to (α, ω) . Therefore, for rigid walls, there is coupling between stable and unstable solutions. Introducing a wall admittance $Y(\omega)$, however, generally breaks these stable–unstable couplings, as the eigenvalues no longer occur in complex conjugate or reflected pairs. This is quite essential in view of the goal of using impedance walls for stabilisation. Exceptions are those impedance models that satisfy $Y^*(\omega) = -Y(\omega^*)$ and both $Y_r(\omega) = 0$ and $Y_i(-\omega) = -Y_i(\omega)$ for $\omega \in \mathbb{R}$ as well as those impedance models that satisfy $Y(-\omega) = -Y(\omega)$ and $Y_r(\omega) = 0$ for $\omega \in \mathbb{R}$. Terms Y_r and Y_i denote the real and imaginary parts of the admittance. While for the first type of impedances the complex conjugation of the eigenvalues is preserved, the second type preserves the reflection of the eigenvalues, as derived in Appendix B. Note that reflection is also given for constant real Y .

2.3. Eigenvalue problem for boundary-layer stability

In this section, we give the analytical solution of the PBE for the exponential boundary layer in terms of the CHF. This solution allows us to convert the differential eigenvalue problem consisting of the PBE (2.3) and the BCs (2.4) and (2.6) into a single algebraic eigenvalue equation. To model the boundary-layer flow, we assume an exponential shear profile, which, non-dimensionalised with U_∞ and δ , reads

$$U_0(y) = 1 - e^{-y}. \tag{2.7}$$

It should be emphasised that with the choice of non-dimensionalisation in this paper, δ does not correspond to the classical definition of the boundary-layer thickness δ_{99} ,

representing the height at which 99 % of the free-stream velocity is reached. Instead, at the wall-normal distance of δ , we have here $U_0 = 1 - e^{-1} \approx 0.63$.

Inserting this profile into the PBE (2.3) yields

$$\frac{d^2 \hat{\rho}}{dy^2} + \frac{2\alpha e^{-y}}{\omega - \alpha (1 - e^{-y})} \frac{d\hat{\rho}}{dy} + \left[M^2 (\omega - \alpha (1 - e^{-y}))^2 - \alpha^2 \right] \hat{\rho} = 0. \quad (2.8)$$

As derived by Zhang & Oberlack (2021) and shown in Appendix C, this equation can be reduced to the confluent Heun differential equation (CHE). Therefore, the general solution for the PBE with exponential profile (2.8) can be given in terms of the CHF, reading

$$\begin{aligned} \hat{\rho}(y) = & C_1 e^{iM\alpha e^{-y} + \sqrt{\theta}y} \cdot \text{HeunC}_1 \left(q, \alpha_H, \gamma, \delta_H, \epsilon, \frac{\alpha}{\alpha - \omega} e^{-y} \right) \\ & + C_2 e^{iM\alpha e^{-y} - \sqrt{\theta}y} \cdot \text{HeunC}_2 \left(q, \alpha_H, \gamma, \delta_H, \epsilon, \frac{\alpha}{\alpha - \omega} e^{-y} \right). \end{aligned} \quad (2.9)$$

Here, $\text{HeunC}_{1/2}(\cdot; z)$ denote the two linearly independent basic power series representations of the CHF, as described in more detail in Appendix C. The far-field exponent is given by

$$\sqrt{\theta} = \sqrt{\alpha^2 - M^2 (\omega - \alpha)^2}, \quad (2.10)$$

describing both the exponential decay and the oscillatory behaviour of the solution in the far field, as is detailed in the next step.

With the exact PBE solution (2.9), we are now in the position to derive an algebraic eigenvalue equation for the eigenvalue problem of the PBE (2.8) with the BCs (2.4) and (2.6). To this end, the BCs are incorporated into the solution (2.9). We start with incorporating the far-field BC $\hat{\rho}(y \rightarrow \infty) = 0$. As $\text{HeunC}(\dots, 0) = 1$ holds (Ronveaux & Arscott 1995), the solution (2.9) simplifies in the far field to

$$\lim_{y \rightarrow \infty} \left(C_1 e^{\sqrt{\theta}y} + C_2 e^{-\sqrt{\theta}y} \right) = 0, \quad (2.11)$$

where the square root of the complex-valued θ is given by

$$\sqrt{\theta} = \frac{\sqrt{2}}{2} \left(\sqrt{\sqrt{\theta_r^2 + \theta_i^2} + \theta_r} + \text{sign}(\theta_i) i \sqrt{\sqrt{\theta_r^2 + \theta_i^2} - \theta_r} \right). \quad (2.12)$$

Since we choose the positive solution branch of the square root function, (2.11) together with (2.12) requires $C_1 = 0$ for the temporal stability case $\omega_i \neq 0$, since this solution branch always grows indefinitely in the far field, giving no physically plausible eigenfunction. Due to the exponential behaviour, $C_1 = 0$ also follows from the more general far-field BC of bounded amplitudes for $\omega_i \neq 0$. The remaining solution branch

$$\hat{\rho}(y) = C_2 e^{iM\alpha e^{-y} - \sqrt{\theta}y} \cdot \text{HeunC}_2 \left(q, \alpha_H, \gamma, \delta_H, \epsilon, \frac{\alpha}{\alpha - \omega} e^{-y} \right) \quad (2.13)$$

is incorporated into the wall BC (2.6). This yields a single determining equation for the eigenvalues (α, ω) fulfilling both the far-field and wall BCs (2.4) and (2.6). This eigenvalue equation is given by

$$\left[\left(-iM\alpha - \sqrt{\theta} \right) + i\omega Y \right] \text{HeunC}_2 \left(; \frac{\alpha}{\alpha - \omega} \right) - \frac{\alpha}{\alpha - \omega} \text{HeunC}_2' \left(; \frac{\alpha}{\alpha - \omega} \right) = 0, \quad (2.14)$$

solved in this paper for the temporal stability eigenvalues $\omega(\alpha; M, Y)$. Note that the prime denotes differentiation of $\text{HeunC}_2(; z)$ with respect to its argument z . Based on the eigenvalue equation (2.14), we examine the boundary-layer stability under the effect of the wall admittance Y both by asymptotic analysis of the eigenvalue equation in § 4 and by numerical solution in § 5. For the evaluation of the CHF in (2.14), we use an implementation in Matlab by Motygin (2018). Further details of this implementation are given in Appendix C.

3. Comparison between the stability of 2-D and 3-D modes

In the previous section, we only considered 2-D modes according to (2.2) which propagate exclusively in streamwise and wall-normal directions. In contrast, 3-D modes also extend in the spanwise z direction. Restricting the stability analysis to 2-D modes is permitted if the most unstable disturbances are 2-D. This is given for rigid-wall boundary layers according to inviscid theory and at almost all finite Reynolds numbers in the case of Mach numbers greater than about 4, where the 2-D second mode is dominant (Mack 1984). The question now arises as to whether this is still valid for boundary layers with impedance walls. In order to clarify this question, we adapt Squire’s idea of an equivalence transformation between the equations for the 2-D perturbations and the equations for the 3-D perturbations. We want to adapt the work of Squire & Southwell (1933) for incompressible viscous shear flows to our problem of compressible inviscid boundary-layer flows. The aim is to derive equivalence relations between the 2-D and 3-D forms of the PBE, from which we can then extract insights into the relationship between the 2-D and 3-D modes.

3.1. Equivalence transformation for the PBE

We start with formulating the normal-mode approach for 3-D perturbations:

$$q(x, y, z, t) = \hat{q}(y)e^{i(\alpha_{3D}x + \beta z - \omega_{3D}t)}, \quad (3.1)$$

where β denotes the spanwise wavenumber in the z direction. With this approach, the PBE for 3-D perturbations can be derived in the same way as before, reading

$$\frac{d^2 \hat{\rho}}{dy^2} + \frac{2\alpha_{3D}}{\omega_{3D} - U_0\alpha_{3D}} \frac{dU_0}{dy} \frac{d\hat{\rho}}{dy} + \left[M_{3D}^2(\omega_{3D} - U_0\alpha_{3D})^2 - k^2 \right] \hat{\rho} = 0, \quad (3.2)$$

with $k^2 = \alpha_{3D}^2 + \beta^2$. Comparison of (3.2) with the 2-D PBE (2.3),

$$\frac{d^2 \hat{\rho}}{dy^2} + \frac{2\alpha_{2D}}{\omega_{2D} - U_0\alpha_{2D}} \frac{dU_0}{dy} \frac{d\hat{\rho}}{dy} + \left[M_{2D}^2(\omega_{2D} - U_0\alpha_{2D})^2 - \alpha_{2D}^2 \right] \hat{\rho} = 0, \quad (3.3)$$

reveals a comparable structure of the two latter equations, suggesting the existence of an equivalence transformation. The subscripts ‘2D’ and ‘3D’ indicate that the equations describe the two-dimensionally and three-dimensionally evolving perturbations, respectively. Here, M_{2D} denotes the Mach number at which the 2-D modes occur, whereas M_{3D} is the Mach number for the 3-D modes. This means that equations (3.3) and (3.2) describe two different solution spaces. In order to transfer solutions between these solution spaces, so-called equivalence transformations for the PBE are required, by which the 2-D and 3-D equations become form invariant.

For the 2-D and 3-D representations (3.3) and (3.2) of the PBE to be form invariant, the quantities that hold specifically for the 2-D and 3-D solution space must fulfil the relations

$$k^2 = \alpha_{3D}^2 + \beta^2 = \alpha_{2D}^2, \tag{3.4a}$$

$$M_{2D}^2 (\omega_{2D} - U_0 \alpha_{2D})^2 = M_{3D}^2 (\omega_{3D} - U_0 \alpha_{3D})^2, \tag{3.4b}$$

$$\frac{\alpha_{2D}}{\omega_{2D} - U_0 \alpha_{2D}} = \frac{\alpha_{3D}}{\omega_{3D} - U_0 \alpha_{3D}}. \tag{3.4c}$$

Combining (3.4b) and (3.4c) yields

$$\frac{M_{2D}^2}{M_{3D}^2} = \frac{\alpha_{3D}^2}{\alpha_{2D}^2} = \Psi^2, \tag{3.5}$$

where $\Psi = M_{2D}/M_{3D}$ is introduced for the Mach number ratio between the 2-D and 3-D solution space. Using Ψ , the transformation relations (3.4) can be written as

$$\alpha_{3D} = \pm \Psi \alpha_{2D}, \quad \omega_{3D} = \pm \Psi \omega_{2D}, \tag{3.6a}$$

$$\beta = \pm \sqrt{1 - \Psi^2} \alpha_{2D}. \tag{3.6b}$$

Equations (3.6) form an equivalence transformation of the PBE, which means that they convert the 3-D PBE (3.2) into the 2-D PBE (3.3). For temporal stability considerations, which presuppose $\alpha, \beta \in \mathbb{R}$, the β -relation (3.6b) leads to the restriction $\Psi < 1$.

The advantage of the equivalence transformation (3.6) is that it allows 3-D eigenvalues ($\alpha_{3D}, \beta, \omega_{3D}$) at Mach number M to be derived from 2-D eigenvalues (α_{2D}, ω_{2D}) at a lower Mach number $\Psi \cdot M$. The shift of the Mach number becomes clear when inserting transformation (3.6) into the 3-D PBE (3.2), giving

$$\frac{d^2 \hat{\rho}}{dy^2} + \frac{2\alpha_{2D}}{\omega_{2D} - U_0 \alpha_{2D}} \frac{dU_0}{dy} \frac{d\hat{\rho}}{dy} + \left[(M \cdot \Psi)^2 (\omega_{2D} - U_0 \alpha_{2D})^2 - \alpha_{2D}^2 \right] \hat{\rho} = 0. \tag{3.7}$$

Furthermore, by means of (3.6), an infinite number of 3-D solutions can be obtained from one 2-D solution set by varying the Mach number ratio Ψ .

To ensure that the transformation (3.6) of the PBE constitutes an equivalence transformation of the full eigenvalue problem, the BCs also have to be taken into account. For 2-D perturbations the BCs read

$$\lim_{y \rightarrow \infty} \hat{\rho}(y) = 0, \tag{3.8}$$

$$\left. \frac{d\hat{\rho}}{dy} \right|_{y=0} = -i \omega_{2D} \hat{\rho}(0) Y(\omega) |_{\omega=\omega_{2D}}, \tag{3.9}$$

as already derived in the previous section. To convert the BCs into the 3-D solution space, we insert the transformation (3.6). This leaves the far-field BC (3.8) unchanged. The BC at the wall, on the other hand, is modified to

$$\left. \frac{d\hat{\rho}}{dy} \right|_{y=0} = \pm i \Psi^{-1} \omega_{3D} \hat{\rho}(0) Y(\omega) |_{\omega=\mp \Psi^{-1} \omega_{3D}}, \tag{3.10}$$

where the parameter Ψ now appears. Only in the case of rigid walls with $Y = 0$ is the wall BC equivalent in the 2-D and 3-D space. Therefore, only for rigid walls does (3.6) constitute an equivalence transformation of the eigenvalue problem. Consequently, the following conclusions from the equivalence transformation only apply to rigid-wall boundary layers.

3.2. Conclusions for rigid-wall boundary layers

The equivalence transformation allows us to deduce conclusions regarding the stability behaviour of the 2-D compared with the 3-D modes. We discuss two aspects in the following. Firstly, we deduce a statement regarding the critical Mach numbers for the occurrence of 2-D and of 3-D instabilities. Secondly, we derive a condition under which 2-D modes represent the most unstable flow perturbations.

The term critical Mach number M_{crit} refers to the Mach number above which a certain instability mode occurs, analogous to the critical Reynolds number in the viscous case. From the transformation for the Mach numbers (3.5) with the constraint $\Psi < 1$ in the temporal stability case, it can now be seen that if such a critical Mach number exists for a certain instability, then the critical 2-D Mach number $M_{\text{crit}, 2\text{D}}$ for the occurrence of the 2-D evolving instability is smaller than the critical 3-D Mach number $M_{\text{crit}, 3\text{D}}$ for the corresponding 3-D instability. This means that 2-D instabilities occur at a lower physical Mach number than 3-D instabilities.

In addition to the latter conclusion about the critical Mach number, it is also possible to use the equivalence transformation to obtain a condition under which among all modes the most unstable one is 2-D evolving. This situation can be described by the relation

$$\omega_{2\text{D},i,\text{max}}|_M > \omega_{3\text{D},i,\text{max}}|_M, \quad (3.11)$$

which says that the maximum growth rate $\omega_{2\text{D},i,\text{max}}$ of all 2-D modes over all wavenumbers at Mach number M should be greater than the maximum growth rate $\omega_{3\text{D},i,\text{max}}$ of all 3-D modes at the same Mach number. Thus, (3.11) describes the case where in a flow with physical Mach number M , the most unstable mode is 2-D.

Applying transformation (3.6) allows us to express the most unstable 3-D growth rates in terms of the most unstable 2-D growth rates according to

$$\omega_{3\text{D},i,\text{max}}|_M = \Psi \omega_{2\text{D},i,\text{max}}|_{(M_{2\text{D}}=\Psi \cdot M)}. \quad (3.12)$$

With (3.12), (3.11) can be written completely in the 2-D solution space in the form

$$\frac{\omega_{2\text{D},i,\text{max}}|_M}{\omega_{2\text{D},i,\text{max}}|_{(\Psi \cdot M)}} > \Psi, \quad (3.13)$$

where $\omega_{2\text{D},i,\text{max}}|_M$ denotes the most unstable 2-D growth rate at Mach number M and $\omega_{2\text{D},i,\text{max}}|_{(\Psi \cdot M)}$ the most unstable 2-D growth rate at smaller Mach number $\Psi \cdot M$. Therefore, if condition (3.13) is fulfilled for all $\Psi \in (0, 1)$, requirement (3.11) is met that the most unstable mode is 2-D evolving. Equation (3.13) thus provides a condition allowing one to assess on the basis of the 2-D modes alone whether they are dominant. In this case, considering only 2-D perturbations is permissible. It is noted that condition (3.13) is obviously fulfilled if $\omega_{2\text{D},i,\text{max}}|_M$ grows monotonically for M .

It should be recalled, however, that the equivalence transformation and therefore the latter conclusions only hold for the case of boundary layers with rigid walls. As soon as an impedance wall with $Y \neq 0$ is introduced, the transformations no longer represent equivalence relations of the eigenvalue problem. Thus, condition (3.13) is not applicable in the case of $Y \neq 0$, making the occurrence of more unstable 3-D modes conceivable.

4. Small-wavenumber asymptotics

It is of particular interest to investigate large-scale streamwise structures, which are characterised by small streamwise wavenumbers α . For this purpose, we perform an asymptotic analysis for small α for our eigenvalue problem. Our aim is to investigate

whether there are designated impedance values for which the stability of the occurring eigenvalues changes significantly. The analytical results thus complement the numerical results in § 5 and allow a more comprehensive insight to be gained into the influence of the impedance on the boundary-layer stability.

For the case of boundary layers with rigid walls, an asymptotic analysis of the associated stability eigenvalue problem has already been performed by Zhang & Oberlack (2021). In comparison with their work, we now want to carry out the asymptotics for the extended problem with wall impedances. Similar asymptotic investigations for flows with wall impedances have already been carried out by Rienstra (2003) and Brambley (2013). Brambley in particular assumes asymptotically small boundary-layer thicknesses, which are equivalent to a small-wavenumber consideration due to the non-dimensionalisation. He obtains a quadratic dispersion relation for constant impedances or a cubic relation for a mass–spring–damper model.

For the asymptotic analysis in the following, we restrict ourselves to the consideration of constant admittances Y , since we are primarily interested in general trends regarding the effects of impedance. In general, however, the asymptotic method can also be applied to impedance models in the same way as described subsequently.

4.1. Leading-order eigenvalue equation

For an asymptotic analysis of the eigenvalues ω for small wavenumbers α , a power series expansion of ω in the small parameter α is formulated according to

$$\omega = a_1\alpha + a_2\alpha^2 + a_3\alpha^3 + \dots + a_n\alpha^n + O(\alpha^{n+1}). \quad (4.1)$$

The constant coefficients a_m , $m = 1, 2, \dots, n$ are to be determined in such a way that (4.1) provides a good approximate solution of the eigenvalue equation (2.14) for small α . To this end, (4.1) is inserted into the eigenvalue equation (2.14) and all terms of the equation are then developed as a power series in α . This requires a series expansion of the CHF in (2.14), as presented in Appendix D.1. By subsequently collecting the coefficients of the powers of α in the resulting eigenvalue equation, algebraic equations for determining the coefficients a_m as functions of M and Y are obtained. Inserting these coefficients a_m back into the asymptotic approach (4.1) provides an eigenvalue approximation for small α . For a more detailed explanation of the procedure for the asymptotic analysis, refer to Appendix D.1.

In the context of this asymptotic analysis, it is assumed that the terms of higher-power-order of α are negligible due to the consideration of small wavenumbers α . We therefore restrict ourselves in the following to the investigation of eigenvalues ω , which are dominated by the leading-order term of the expansion (4.1), meaning $\omega \approx a_1\alpha$. We denote these leading-order eigenvalues by $\omega^{(1)}$, i.e.

$$\omega^{(1)} = a_1\alpha. \quad (4.2)$$

It should be noted that the neglect of the higher-order terms requires assumptions on the convergence of the power series representation of the Heun function, as discussed in Appendix D.2.

To determine the coefficients a_1 of the leading-order eigenvalues $\omega^{(1)}$, an algebraic equation is derived according to the procedure of collecting the coefficients of the power of α described in Appendix D.1. This equation for a_1 can be written in the form

$$f_1(a_1; M, Y) = a_1 \left(a_1 \sqrt{1 - (a_1 - 1)^2 M^2} - iY(a_1 - 1)^2 \right) = 0. \quad (4.3)$$

The notation f_1 refers to (D4) in Appendix D. It should be noted that for $Y = 0$ equation (4.3) reduces to a form equivalent to the equation in Zhang & Oberlack (2021). Due

to the branching behaviour of the root functions in (4.3), the solutions a_1 determining the leading-order eigenvalues (4.2) behave in a branching manner depending on the parameters M and Y . We therefore want to examine how the solutions a_1 and thus the leading-order eigenvalues $\omega^{(1)}$ change under variation of Y , with a focus on possible branching which can lead to a change in the number and character of the eigenvalues (§ 4.3). For this purpose, we first classify the different solutions $a_1(Y, M)$ of (4.3) in order to determine the Y values depending on M at which branching occurs (§ 4.2). This root classification is based on a reduction of (4.3) to a quartic function, similar to the work of Rienstra (2003), where the asymptotic approximation yields a quartic function that allows a classification of the number and character of the surface modes.

4.2. Root classification of the leading-order term

The aim is to formulate criteria for classifying the roots a_1 determining the leading-order eigenvalues $\omega^{(1)}$. To do this, we consider the leading-order equation (4.3), where we truncate the outer factor a_1 , giving the trivial solution. Converting the latter equation by bringing the term $iY(a_1 - 1)^2$ to the right-hand side of the equation and subsequently squaring it, we obtain a quartic equation for a_1 in the form

$$(M^2 - Y^2)a_1^4 + (-2M^2 + 4Y^2)a_1^3 + (M^2 - 6Y^2 - 1)a_1^2 + 4Y^2a_1 - Y^2 = 0. \quad (4.4)$$

It should be noted that squaring can lead to additional solutions. Therefore, to filter out incorrect solutions, the solutions of (4.4) have to be subsequently reinserted into (4.3). In order to derive classification criteria, (4.4) is transformed in the next step according to Dickson (1914) to a reduced form without cubic term. For this, we employ the transformation

$$a_1 = \tilde{a}_1 - \frac{b}{4} \quad \text{with} \quad b = \frac{(-2M^2 + 4Y^2)}{M^2 - Y^2}, \quad (4.5)$$

where b results from the coefficient of the cubic term in (4.4) divided by the coefficient of the highest power. Applying (4.5) to (4.4) yields the reduced quartic equation

$$\tilde{a}_1^4 + q\tilde{a}_1^2 + r\tilde{a}_1 + s = 0. \quad (4.6)$$

The coefficients q, r, s of (4.6) are specified as functions of M and Y according to

$$q = \frac{-M^4 + (-2Y^2 - 2)M^2 + 2Y^2}{2(M^2 - Y^2)^2}, \quad (4.7a)$$

$$r = \frac{(Y^2 - 1)M^4 + 3M^2Y^2 - 2Y^4}{(M^2 - Y^2)^3}, \quad (4.7b)$$

$$s = \frac{M^8 + (-4Y^2 - 4)M^6 + 20M^4Y^2 - 32M^2Y^4 + 16Y^6}{16(M^2 - Y^2)^4}, \quad (4.7c)$$

having the singularities $Y = \pm M$ induced by b in (4.5).

For real coefficients q, r, s , which are given according to (4.7) in the case of real admittances $Y \in \mathbb{R}$, the reduced form (4.6) allows us to formulate criteria to classify its roots \tilde{a}_1 based on the discriminant Δ (see Rees 1922). For the reduced quartic polynomial (4.6), the discriminant can be expressed in the form (Prodanov 2022)

$$\Delta = 16q^4s - 4q^3r^2 - 128q^2s^2 + 144qr^2s - 27r^4 + 256s^3. \quad (4.8)$$

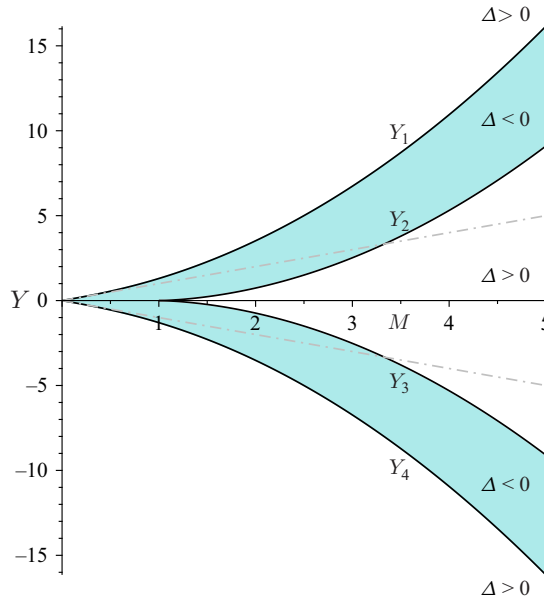


Figure 1. Sign of the discriminant Δ as main classification criterion: real roots Y_j , $j = 1, \dots, 4$ (black curves), where $\Delta = 0$, dividing $\Delta > 0$ (white areas) and $\Delta < 0$ (blue areas); singularities at $Y = \pm M$ (dot-dashed grey lines).

Using the relations (4.7), Δ is obtained as a function of the parameters M and Y :

$$\Delta = \frac{16Y^2 [16Y^4 + (-8M^4 - 20M^2 + 1)Y^2 + (M^8 - 3M^6 + 3M^4 - M^2)]}{(M - Y)^6(M + Y)^6}. \quad (4.9)$$

As stated in Rees (1922), the roots \tilde{a}_1 of (4.6) can now be classified in terms of number and character by means of the sign of the discriminant Δ . As a consequence, the number or character of the roots \tilde{a}_1 only changes at the zeros of Δ , which thus represent branch points of the solutions \tilde{a}_1 . From (4.9), the non-trivial zeros of Δ can be found at

$$Y_{1,4} = \pm \frac{\sqrt{-2 + 16M^4 + 40M^2 + 2\sqrt{(8M^2 + 1)^3}}}{8} \quad \text{for } M \geq 0, \quad (4.10a)$$

$$Y_{2,3} = \pm \frac{\sqrt{-2 + 16M^4 + 40M^2 - 2\sqrt{(8M^2 + 1)^3}}}{8} \quad \text{for } M \geq 1. \quad (4.10b)$$

The restriction of $Y_{2,3}$ to $M \geq 1$ follows from the fact that the classification criteria only apply for real admittances Y , as explained above. The key point now is that, due to (4.5), the classification criteria for the solutions \tilde{a}_1 apply analogously to the solutions a_1 determining the leading-order eigenvalues $\omega^{(1)}$. Consequently, branching of the leading-order eigenvalues $\omega^{(1)}$ occurs at precisely these values Y_j given by (4.10).

In figure 1, the branching points Y_j as a function of M are shown as black lines, along which $\Delta = 0$. They divide the parameter space (M, Y) into areas $\Delta > 0$ and $\Delta < 0$. Additionally, the singularities $Y = \pm M$ of the discriminant are plotted as grey dot-dashed lines. We see that in the subsonic case $M < 1$ only the two branching points $Y_{1,4}$ occur, while the further branching points $Y_{2,3}$ only arise for $M > 1$ according to (4.10). In addition, it can be seen that the branching point lines are symmetric to the $Y = 0$ axis,

which indicates that the eigenvalues have the same branching behaviour for passive walls $Y > 0$ as for active walls $Y < 0$. This is consistent with the result of the symmetry analysis in [Appendix B](#), where we found that the transformation (B13) represents a symmetry of the eigenvalue problem for constant real admittances Y , from which it follows that the eigenvalues for $-Y$ result from the eigenvalues for Y by reflection. This implies that the solutions for Y and $-Y$ have the same branching behaviour.

Regarding the results in this section, it should be emphasised again that squaring the leading-order term to convert it into a fourth-order polynomial has led to an expansion of the solution space. This means that potentially not all solutions of the fourth-order polynomial (4.4), on which the root classification is based, are in fact solutions a_1 of the leading-order equation (4.3), implying that less than four asymptotic eigenvalues $\omega^{(1)}$ occur. Indeed, this is what we observe in the following subsection, where we consider the leading-order eigenvalues $\omega^{(1)}$ for different Mach numbers M under variation of Y . Nevertheless, the achievement of the classification to exactly predict the occurrence of eigenvalue branch points is of key importance and manifests itself in the results for $\omega^{(1)}$ in the next subsection.

4.3. Leading-order eigenvalues under admittance variation

Based on the previous asymptotic expansion, we now calculate the eigenvalues for small wavenumbers α . Again, we focus on the leading-order eigenvalues $\omega^{(1)}$, given by the coefficients $a_1 = \omega^{(1)}/\alpha$ according to (4.2). Thus, we determine the solutions a_1 of the leading-order eigenvalue equation (4.3) for different Mach numbers M under variation of the admittance Y . Here we restrict ourselves to constant real admittances in order to be able to compare the results with the predictions of the root classification in the previous section. In the following, we are particularly interested in whether new instability modes can occur due to the wall admittance Y . According to the previous section, such an emergence of new leading-order modes $\omega^{(1)}$ is to be expected for certain admittance values, the discussed branching points Y_j .

[Figure 2](#) shows for three different Mach numbers ($M = 0.8$, $M = 2$, $M = 4.2$) the solutions a_1 plotted as curves over increasing positive real Y , starting from the rigid-wall case $Y = 0$. In order to be able to identify the effects of Y on both the stability and the phase velocity of the modes, we have plotted the imaginary part (left-hand panels) and the real part (right-hand panels) of the solutions a_1 separately over Y . Therefore, the left-hand panels provide information about the temporal growth rates $a_{1,i} = \omega_i^{(1)}/\alpha$ of the leading-order modes, while the right-hand panels show the corresponding phase velocity $a_{1,r} = \omega_r^{(1)}/\alpha$. The individual solutions a_1 are plotted in different colours to allow assignment of the real parts $a_{1,r}$ to the corresponding imaginary parts $a_{1,i}$.

To validate the results a_1 of the small-wavenumber asymptotics, we also solved the eigenvalue equation numerically to a small wavenumber $\alpha = 10^{-3}$. Here, several admittance values Y were considered for all three Mach numbers $M = 0.8$, $M = 2$, $M = 4.2$. These numerical solutions ω/α are plotted in [figure 2](#) as black crosses.

[Figure 2](#) reveals that the behaviour and the number of asymptotic solutions a_1 change at selected admittance values, marked on the abscissa by black squares and black diamonds. The black square indicates the singularity $Y = M$ in the leading-order equation (4.3). Here, an additional solution (green) with vanishing imaginary part $a_{1,i} = 0$ occurs, as can be observed for all three Mach-number cases. It should be noted at this point that for the asymptotic expansion (4.1) applied to the eigenvalue equation (2.14), real solutions only arise in the leading order a_1 . The solutions of the higher-order terms a_m , $m \geq 2$, however, always have imaginary parts, resulting in the asymptotic eigenvalue (4.1) being complex in total. Consequently, the solutions a_1 with vanishing imaginary part $a_{1,i} = 0$ only represent

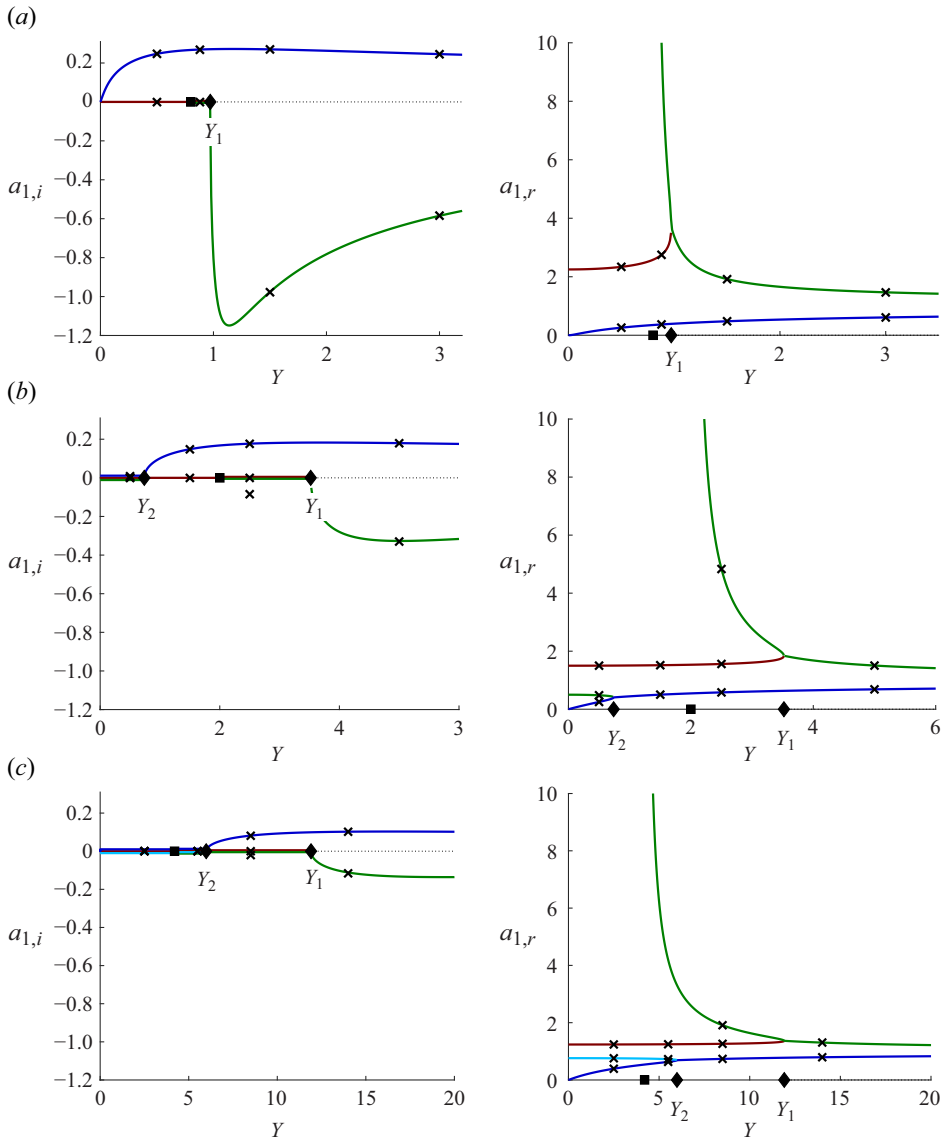


Figure 2. Solutions a_1 for leading-order eigenvalues $\omega^{(1)}$ plotted over positive wall admittance Y : imaginary parts $a_{1,i}$ (left), real parts $a_{1,r}$ (right). Symbols \blacklozenge and \blacksquare : branching points Y_1 , Y_2 and singularity $Y = M$. Mach numbers (a) $M = 0.8$, (b) $M = 2$ and (c) $M = 4.2$.

neutrally stable eigenvalues in the leading order, referred to in the following as neutrally stable leading-order eigenvalues. The black diamonds in figure 2 mark the branching points, given by (4.10), which were derived from the root classification in the previous section. According to (4.10), there are two positive branching points Y_1 , Y_2 for $M > 1$ (see figure 2b,c), whereas there is only the one branching point Y_1 for $M < 1$ (see figure 2a).

4.3. Stability of the leading-order eigenvalues

For both supersonic cases $M = 2$ and $M = 4.2$ we observe from the left-hand panels for the growth rates $a_{1,i}$ that for small admittances $Y < Y_2$ only real, i.e. neutrally stable,

leading-order eigenvalues occur. At the branching point Y_2 , however, the solutions branch, causing the emergence of a solution with positive growth rate $a_{1,i} > 0$ (royal blue). Consequently, Y_2 represents a critical admittance value, which leads to a new unstable mode at small wavenumbers α according to the asymptotics. This is a decisive result for the design of acoustic wall coatings intended to delay the boundary-layer transition. When increasing the admittance Y beyond Y_2 , the growth rate of the unstable mode increases to saturation. At the higher branching point Y_1 , a new solution with a negative growth rate $a_{1,i} < 0$ (green) emerges from the remaining neutrally stable solutions, which represents a stable mode.

Comparison of [figure 2\(b\)](#) for $M = 2$ and [figure 2\(c\)](#) for $M = 4.2$ shows that the leading-order eigenvalues for different supersonic Mach numbers behave similarly under variation of Y . However, we see that the new instability (royal blue), occurring for admittances $Y > Y_2$, has a higher maximum growth rate in the case of the smaller Mach number, namely $a_{1,i,\max} \approx 0.18$ for $M = 2$ compared with $a_{1,i,\max} \approx 0.1$ for $M = 4.2$. In addition, a smaller M leads to the branching points Y_1 and Y_2 occurring earlier, i.e. for smaller admittance values, which is consistent with [figure 1](#) in the previous section, showing the branching points over the Mach number. As a result, in boundary layers with lower Mach numbers, the critical value Y_2 is exceeded earlier; thus the new instability occurs from smaller admittances.

In the subsonic case $M < 1$, branching of the asymptotic eigenvalues a_1 only occurs at Y_1 , as formula (4.10) reveals. This is where the new stable mode (green) emerges (see [figure 2a](#)). The new unstable mode, on the other hand, directly occurs for all positive wall admittances $Y > 0$ and reaches here for $M = 0.8$ a maximum growth rate of $a_{1,i,\max} \approx 0.28$, which is higher than in the cases $M > 1$. This is a key result when it comes to the technical use of metasurfaces in areas such as aerospace applications where the operating Mach number changes. The behaviour as in [figure 2\(a\)](#) is similarly found for other subsonic Mach numbers $M < 1$, whereby again the trend is observed that a reduction of M leads to a higher maximum growth rate of the newly occurring instability.

4.3.2. Phase velocity of the leading-order eigenvalues

From the right-hand panels of the real parts $a_{1,r}$, we can observe at the branching points merging of the phase velocities of two neutrally stable modes in all Mach-number cases. Furthermore, it can be seen at all Mach numbers that the newly occurring instability (royal blue) has a phase velocity $a_{1,r}$ in the range $[0, 1]$. Due to the scaling with U_∞ , the velocities 0 and 1 correspond to the minimum and maximum velocity of the mean flow. This means that for the instability modes with $a_{1,r} \in [0, 1]$ there exists a critical layer where the phase velocity is equal to the local mean flow velocity. Here, according to critical layer theory (Maslowe 1986), optimal energy exchange takes place between the mean flow and the disturbance, which causes unstable acceleration. The new stable solution (green), on the other hand, propagates with phase velocity $a_{1,r} > 1$. Near the branching point Y_1 , the stable solution even shows $a_{1,r} > 1 + 1/M$, which corresponds to $\tilde{\omega}_r/\tilde{\alpha} > U_\infty + c$ in dimensional representation. Accordingly, it is partially supersonic, propagating faster than the speed of sound c relative to the free-stream velocity U_∞ (Mack 1990).

Comparing the asymptotic leading-order solutions a_1 with the numerical eigenvalues ω/α (black crosses) at the different Y values shows extremely good agreement. In particular, the occurrence of the new instability from $Y > Y_2$ for $M > 1$ or from $Y > 0$ for $M < 1$ can also be seen in the numerics. The only difference between the numerical and asymptotic results is the starting point of the stable solution. We observe that in the numerics the stable solution already occurs for values $Y < Y_1$ in the supersonic cases (see

left-hand panels of figure 2*b,c*). The reason for this deviation could be the neglect of the higher-order terms in the asymptotic analysis. Apart from this, the numerical eigenvalues agree to very high accuracy with the asymptotic results shown in this section, in terms of both growth rate and phase velocity.

5. Numerical solutions of the full eigenvalue problem

This section intends to shed light on the effects of acoustic metasurfaces on the eigenmodes in high-velocity boundary-layer flows. While the asymptotic analysis for large streamwise structures in the previous section focused on small streamwise wavenumbers, we now extend the investigations to a broad wavenumber spectrum.

In addition to the stabilisation of the second mode by metasurfaces, as observed in previous studies such as Malmuth *et al.* (1998) or Fedorov *et al.* (2003), we are particularly interested in the emergence of new unstable modes above critical wall impedance values, as predicted by the asymptotics. Furthermore, we compare the growth of the 2-D and 3-D instabilities, given the question of the direction of dominant growth.

In this section, we first consider constant real impedances (§ 5.2), with the aim of identifying the fundamental effects of wall impedance and proving consistency with the asymptotic analysis for small α . The findings are compared with the rigid-wall reference case. Subsequently, an impedance model for porous walls is applied, as they provide a technically relevant example of metasurfaces (§ 5.3).

The results in this section were obtained by numerically solving the underlying algebraic eigenvalue equation of the problem, which for the 2-D modes reads as (2.14), as derived in § 2. The eigenvalue equation for the 3-D modes, which can be deduced analogously from the PBE (3.2) and the BCs (3.8), (3.10) in the 3-D solution space, corresponds to the 2-D eigenvalue equation (2.14) with θ extended by the spanwise wavenumber β to

$$\theta = -M^2 (\omega - \alpha)^2 + \alpha^2 + \beta^2. \quad (5.1)$$

By solving the eigenvalue equation for varying wall impedance over a broad Mach number and wavenumber spectrum, the physical effects of metasurfaces described above are to be comprehensively investigated, thus complementing the observations of the theoretical analyses in the previous sections.

5.1. Numerical solution scheme

Before discussing the results, the numerical method used to solve the eigenvalue equation is briefly explained in advance. As discussed in Appendix C, the exact solution occurring in the eigenvalue equation (2.14) contains the CHF. Since the eigenvalue equation represents the impedance wall BC, it requires the evaluation of the CHF at the wall, i.e. at $y = 0$. For this evaluation, we use a Matlab implementation of the CHF, developed by Motygin (2018). As this implementation has branch cuts on the real axis, the argument of the CHF, $z = \alpha/(\alpha - \omega)$ in the present work, must have an imaginary part. This is obviously the case if stable or unstable modes with $\omega_i \neq 0$ are considered. Vice versa, no conclusions on neutrally stable modes are made in this work and we focus on stable and unstable modes.

These modes are given as complex zeros $\omega = \omega_r + i \omega_i$ of the complex eigenvalue equation for a given set of parameters α , M , Y . Due to the structure of the eigenvalue equation with ω occurring in both the parameters and the argument of the CHF, it cannot be resolved explicitly for ω . Therefore, eigenvalues are determined numerically by a sign change algorithm. It uses the fact that the eigenvalues are given at points where in the vicinity both the imaginary and the real parts of the eigenvalue equation change their

Parameters	Inviscid EV	Viscous EV
$M = 4.2, \alpha = 1.5$	$1.1073 + 0.00841i$	$1.1066 + 0.00842i$
$M = 5, \alpha = 1.5$	$1.0279 + 0.01077i$	$1.0281 + 0.01070i$
$M = 3, \alpha = 2$	$1.5559 + 0.00235i$	$1.5536 + 0.00299i$

Table 1. Validation of the most unstable inviscid eigenvalue (EV) from the sign change algorithm with a re-iteration using the Mueller algorithm against the most unstable viscous EV from the collocation method for different parameters at $Y = 0$.

sign. Consequently, the search domain is discretised first, yielding a grid in ω_r and ω_i . Thereafter, sign changes are detected on the grid. However, the precision of the eigenvalues found this way depends on the refinement of the grid. Therefore, to improve the precision of the results, the solutions of the sign change algorithm are subsequently used as initial guesses for a Mueller algorithm. This is a root-finding algorithm similar to the Newton method, but with convergence of almost order 2. With this calculation method, we ensure high precision and avoid the occurrence of spurious modes.

In order to verify the results, we compare them in selected cases with eigenvalues from a collocation method, adapted for an isothermal boundary layer. Since inviscid equations include various singularities, collocation methods would fail if applied on these equations. Therefore, we validate against results from the viscous compressible linearised Navier–Stokes equations at very high Reynolds number $Re = 2 \times 10^7$. For this purpose, a Chebyshev collocation method is applied to the viscous boundary-layer stability problem, where again the base flow is assumed to be isothermal with the exponential main flow profile (2.7). The BCs are set as follows: in addition to the impedance wall BC (2.6), no-slip as well as vanishing temperature fluctuations are assumed at the wall. In the far field it is demanded that the perturbations vanish according to (3.8). Stretching the Chebyshev domain (Schmid & Henningson 2001) allows half of the collocation points to be set below a certain limit in order to resolve the near-wall region, in which larger gradients of the eigenfunctions occur, more accurately. The number of collocation points is set to 250. Further details of the method and an application to non-isothermal boundary-layer flows over highly cooled impedance walls can be found in De Broeck *et al.* (2022).

The results from both calculations show very good agreement for the most unstable eigenvalues, deviating only of $\mathcal{O}(10^{-3})$ with respect to ω_r and $\mathcal{O}(10^{-4})$ with respect to ω_i . Also for smaller Reynolds numbers, such as $Re = 10^5$, the results agree quite well. Examples for the most unstable eigenvalues resulting from both calculation methods in the case of a rigid wall are given in table 1.

5.2. Results for constant wall admittances

Using the method based on the sign change and Mueller algorithm described above, we examine the effects of constant real wall admittances Y in this section. The results presented hereinafter are structured as follows. First, we investigate the admittance effects on the 2-D modes in supersonic boundary layers (§ 5.2.1). The new instability observed for a sufficiently large admittance value Y is subsequently investigated in more detail with respect to the critical admittance value leading to its emergence (§ 5.2.2). Finally, the unstable growth of 2-D modes and 3-D modes is compared, whereby we consider both the original boundary-layer instability modes and the newly occurring instability (§ 5.2.3).

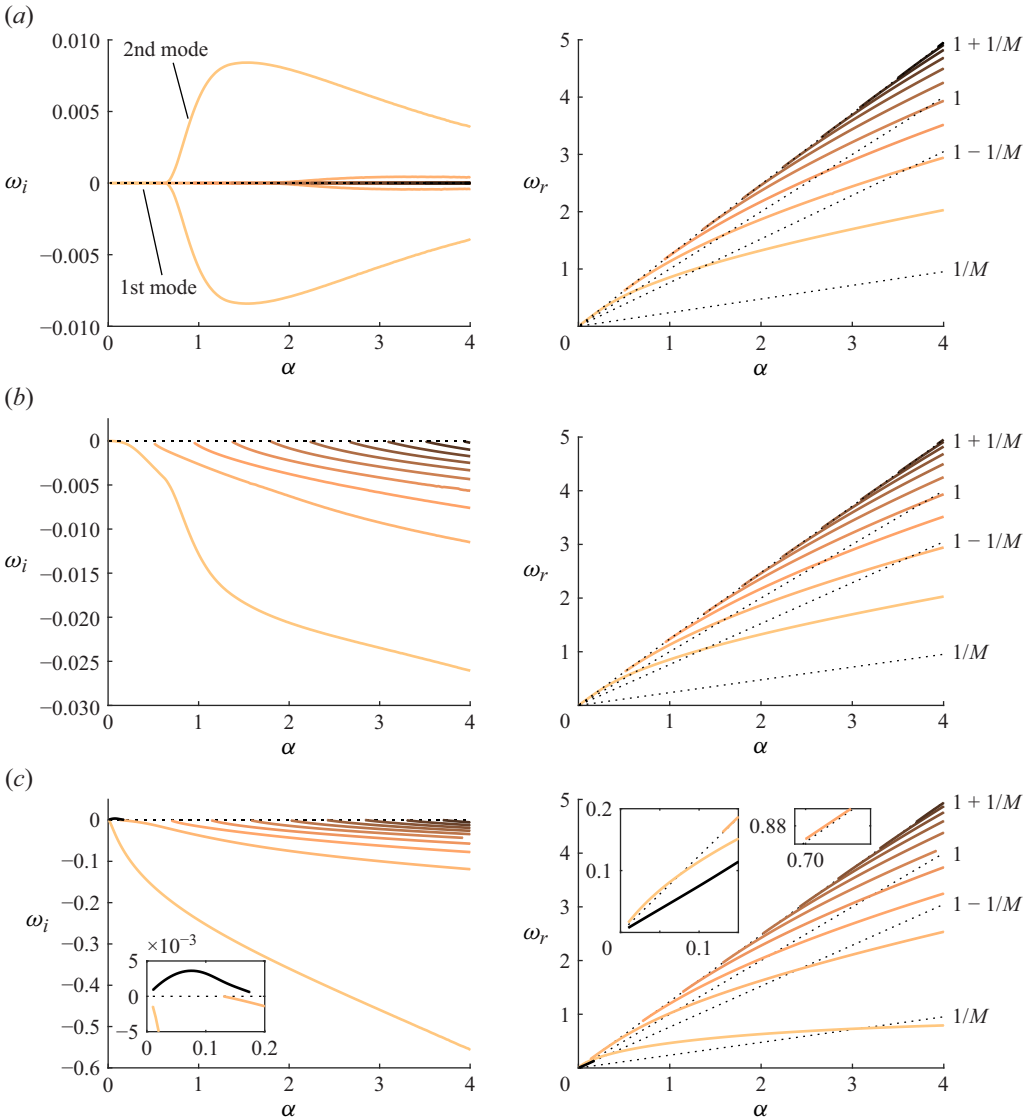


Figure 3. Growth rate ω_i (left) and frequency ω_r (right) of the 2-D perturbations plotted over wavenumber α for Mach number $M = 4.2$ and three different constant wall admittances Y : (a) rigid wall $Y = 0$, (b) $Y = 0.2$, (c) $Y = 10$.

5.2.1. Damping effect and occurrence of a new instability for 2-D modes

The influence of metasurfaces on the stability and the phase velocity of all modes in high-velocity boundary layers should be fundamentally examined, focusing here first on the 2-D modes. For this purpose, we compare the 2-D eigenmodes for constant admittances $Y \neq 0$ with those in the rigid-wall case $Y = 0$ with regard to their temporal growth rate ω_i and frequency ω_r .

In figure 3, the imaginary part ω_i and real part ω_r of the eigenvalues ω in the Mach $M = 4.2$ boundary layer are plotted separately over the streamwise wavenumber α for three admittance values: $Y = 0$, $Y = 0.2$, $Y = 10$.

The left-hand panels showing ω_i over α reveal that in the rigid-wall case $Y = 0$ the unstable and stable solutions occur in a complex conjugate manner, as predicted by the symmetry analysis in [Appendix B](#). Further, we observe in the left-hand panel of [figure 3\(a\)](#) the maximum growth of the most unstable mode (plotted in yellow) at $\alpha \approx 1.5$, i.e. at a wavenumber of 1.5 times the boundary-layer thickness. In this context, however, it is crucial to mention that scaling the decay rate of the velocity profile, i.e. introducing the profile $U_0(\frac{1}{c}y)$, leads to scaled eigenvalues and eigenfunctions ($(1/c\alpha)$, $(1/c\omega)$, $(c^2\hat{\rho})$), provided that constant admittances Y are assumed (see [Appendix E](#)). In other words, scaling the results $(\alpha, \omega, \hat{\rho})$ with a constant factor again yields eigenvalues and eigenfunctions of the boundary-layer problem with a rescaled velocity profile. Consequently, the results presented here for constant Y are to be assessed qualitatively in terms of fundamental effects, not quantitatively. In previous experimental studies by [Stetson & Kimmel \(1993\)](#) or [Kimmel *et al.* \(1996\)](#), the maximum growth rate of the second mode was found at a wavenumber of about half the layer thickness.

If we now look at [figure 3\(b,c\)](#) for $Y \neq 0$, we see that the eigenvalues are no longer complex conjugate. Accordingly, the constant admittance breaks this coupling of stable and unstable solutions, as already observed in [Appendix B](#). Furthermore, the left-hand panel of [figure 3\(b\)](#) reveals that a stabilisation of all modes could be achieved by $Y = 0.2$.

When increasing the admittance to $Y = 10$, however, the emergence of a new instability (black) at small wavenumbers can be observed in [figure 3\(c\)](#), which confirms the results from the asymptotics. This phenomenon is of central physical importance and is therefore examined in more detail in the following section.

From the right-hand panels for ω_r over α , it can be seen that in the rigid-wall case $Y = 0$ (see [figure 3a](#)) the modes propagate with phase velocities $\omega_r/\alpha \in [0, 1]$ as soon as they show pronounced unstable growth rates. This is consistent with the critical layer theory as explained previously. The same applies to the newly occurring instability (black) in the case $Y = 10$, which propagates with $\omega_r/\alpha \approx 1 - (1/M)$ (see inset in [figure 3c](#)). Comparing the ω_r - α plots of the three different Y values reveals that the phase velocities of the modes, already initially occurring for a rigid wall, are only slightly affected by the smaller wall admittance $Y = 0.2$. For high wall admittances, such as $Y = 10$, however, we observe an acceleration of the stabilised modes. As a result, they reach phase velocities slightly above $1 + (1/M)$ for small α , as can be seen exemplarily in the insets of the two lowest modes in the right-hand panel of [figure 3\(c\)](#). Further, we see for the two lowest modes that they fall below the $1 - (1/M)$ line for smaller α than in the cases $Y = 0$ and $Y = 0.2$. In dimensional representation, $1 \pm (1/M)$ corresponds to $U_\infty \pm c$, which means that the modes propagate partially supersonically relative to the free-stream velocity.

To assess the character of the instability modes, we consider the associated eigenfunctions with regard to their zero crossings, as described in [Mack \(1984\)](#). For the eigenfunctions, we could derive the exact representation (2.13) from the PBE solution. Plotting the eigenfunctions of the modes in the boundary layer with $Y = 0$ reveals that the dominant instability (yellow) in the rigid-wall case represents a second mode. However, this is only the case for wavenumbers where this dominant mode shows clearly unstable growth. In the range of smaller wavenumbers, on the other hand, where only vanishing small growth rates ω_i occur, this solution represents a first mode. The additional unstable modes with smaller growth rates that occur at higher wavenumbers in the rigid-wall case are further higher acoustic Mack modes. The type of all these modes, which already exist in the rigid-wall boundary layer, does not change when stabilised by wall admittances $Y \neq 0$.

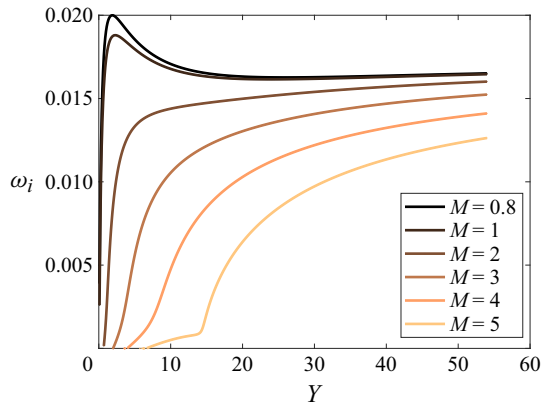


Figure 4. Growth rate ω_i of the new instability plotted over positive wall admittance Y for different Mach numbers.

Of particular interest is the instability emerging for large admittances, which is found to be a first mode. This finding is consistent with previous studies for viscous boundary layers, observing slight destabilisation of the first mode by porous surfaces (Fedorov *et al.* 2003). The results in this work, though, explicitly show for the inviscid case that the first mode, which already occurs for $Y = 0$, is indeed stabilised by wall admittances, like the higher modes. However, as the admittance is increased, the stimulating effect of the wall coating on the first mode becomes apparent, leading to the appearance of a new unstable first mode.

It should be noted that for the characterisation of the modes based on the eigenfunctions' zero crossings, as in Mack (1984), those zero crossings are not taken into account which are caused by the oscillatory behaviour of the far-field solution, as can be seen in the eigenfunction plots in Appendix A. The oscillation of the far-field solution, which is given by (2.11), follows from the fact that the square root of the complex number θ , defined by (5.1), is itself a complex number. This means that the far-field solution can be decomposed according to

$$\hat{\rho}_{ff}(y) = C_2 e^{-\sqrt{\theta}y} = C_2 e^{-((\sqrt{\theta})_r + i(\sqrt{\theta})_i)y}, \tag{5.2}$$

revealing its exponential as well as oscillatory behaviour. Here it is worth noting again that the positive square root branch is selected.

5.2.2. Influence of wall admittance on the new instability

In view of the goal of delaying the boundary-layer transition, the phenomenon of the newly occurring first-mode instability due to certain wall admittances is of great practical importance. Therefore, the behaviour of the growth rate ω_i of the new instability under increasing Y is examined more closely for different Mach numbers in the following (figure 4). In this context, the question arises in particular as to the critical admittance value above which the new instability sets in. The results presented in figure 4 were calculated for the small wavenumber $\alpha = 0.1$.

As figure 4 reveals, for all Mach numbers $M > 1$ the instability actually only emerges in each case from a critical value $Y_{crit,2D}$, which depends on the Mach number. We observe that the value $Y_{crit,2D}$ decreases when M is reduced, meaning that in boundary layers of smaller Mach number, the first-mode instability already occurs at lower admittances. For $M < 1$, the instability even emerges directly from all admittance $Y > 0$. We use

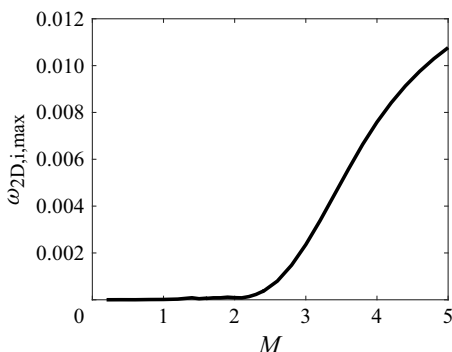


Figure 5. Maximum growth rate $\omega_{2D,i,\max}$ of all 2-D modes plotted over Mach number M for $Y = 0$.

the designation $Y_{\text{crit},2D}$ as the critical value for the occurrence of the 2-D disturbances considered here.

Furthermore, it can be observed that the unstable growth rates ω_i grow when Y is increased beyond the respective critical value $Y_{\text{crit},2D}$. In the subsonic cases $M < 1$, a maximum growth rate occurs at around $Y = 1$ before a saturation rate is reached as Y increases. For all $M > 1$, on the other hand, the growth rate increases monotonically with increasing Y up to the saturation value. Both the saturation growth rate for $Y \rightarrow \infty$ as well as the maximum growth rate in the cases $M < 1$ all prove to be the greater the smaller is M . Accordingly, a decrease of M leads to earlier occurrence and stronger growth of the new first-mode instability.

These findings are consistent with the results of the asymptotics in §4.3, which qualitatively observed the same effects of a reduction of M on the critical admittance value, there given by the branching point Y_2 , and on the saturation growth rate ω_i for large Y (see figures 1 and 2).

5.2.3. Comparison of 2-D and 3-D evolving unstable modes

So far, only 2-D modes have been considered. For a comprehensive understanding of the influence of metasurfaces on the boundary-layer stability, the question of the growth of 3-D modes compared with that of 2-D modes is addressed in this section. In this context, condition (3.13) has been derived for the dominating instabilities in boundary layers with rigid wall ($Y = 0$) to be 2-D modes. This condition is checked in the following on the basis of the numerical eigenvalues. However, such a condition for 2-D dominance cannot be formulated for admittances $Y \neq 0$, as shown in §3, since for $Y \neq 0$ the 2-D and 3-D modes are not linked via a transformation. Therefore, we also compare the growth of 2-D and 3-D modes in the case $Y \neq 0$.

To check condition (3.13) for dominance of the 2-D instability perturbations in the rigid-wall boundary layer, figure 5 shows the maximum growth rate $\omega_{2D,i,\max}$, which occurs under all 2-D modes for arbitrary wavenumber, plotted against the Mach number M . This was done by numerically calculating all 2-D modes over a broad wavenumber spectrum for varying Mach number. As one can see from figure 5, for $M > 2.4$, $\omega_{2D,i,\max}$ grows monotonically with increasing M and is greater than for all smaller Mach numbers. Therefore, in the considered Mach number range, condition (3.13) is fulfilled for all $M > 2.4$, which implies dominance of the 2-D instabilities.

Since the condition (3.13) does not apply for $Y \neq 0$, we now focus on the new first-mode instability, occurring for admittances $Y > Y_{\text{crit},2D}$. The aim is to examine whether this mode is more unstable for 2-D or 3-D propagation. For this purpose, in figure 6 the

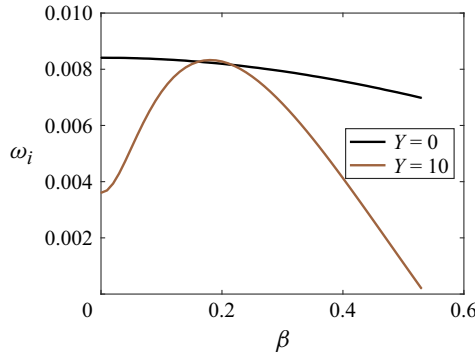


Figure 6. Growth rate ω_i of new instability (brown) for $Y = 10$ and dominant second mode (black) for $Y = 0$ plotted over wavenumber β .

maximum growth rate ω_i of the new instability (brown) is plotted against the spanwise wavenumber β . The results were obtained for $M = 4.2$, $Y = 10$. Wavenumber $\alpha = 0.08$ was chosen as the streamwise wavenumber, as for this the instability shows the maximum growth ω_i when propagating in two dimensions. For comparison, the growth rate ω_i of the dominant second mode, occurring in the rigid-wall boundary layer at $M = 4.2$, is also shown (black). Here, $\alpha = 1.5$ was chosen, representing the point of maximum growth of the 2-D second mode (see figure 3a).

As we can see from figure 6, the second-mode instability of the case $Y = 0$ is most unstable for $\beta = 0$, i.e. when propagating in two dimensions, which confirms condition (3.13). For the newly occurring first-mode instability, on the other hand, maximum growth occurs at $\beta \neq 0$, namely at $\beta \approx 0.2$ for the parameters considered here. This implies that stronger growth occurs in the 3-D than in the 2-D direction. This can be attributed to the character of this instability as first mode. In the direction of maximum growth, the first mode can even reach growth rates of approximately the maximum growth rate of the dominant rigid-wall second mode, as observed here for $Y = 10$ at $M = 4.2$.

5.3. Results for porous wall admittance

So far we have only investigated the effects in the case of constant admittances Y . We now extend our investigations to the practically relevant case of walls with porous coating.

5.3.1. Porous wall model

For the mathematical description of such porous walls, we use a model proposed by Fedorov *et al.* (2001), building on the works of Daniels (1950), Benade (1968) and Stinson & Champoux (1992). According to this model, the porous wall admittance is given by

$$Y = -\frac{\phi}{Z_0} \tanh(\Lambda h). \tag{5.3}$$

Here, h represents the porous-layer thickness and ϕ the porosity. The latter is given by the ratio of the pore radius r to the pore spacing s according to $\phi = \pi(r/s)^2$. Thus, ϕ lies in the range $\phi \in [0, \pi/4]$, since r cannot exceed the limit $r = s/2$. These quantities were scaled with the boundary-layer thickness δ . Parameters Z_0 and Λ describe the characteristic impedance and the propagation constant, which can be expressed by

$$Z_0 = \sqrt{\frac{Z_1}{Y_1}}, \quad \Lambda = \sqrt{Z_1 Y_1}, \quad \text{where } \text{Re}(\Lambda) < 0. \tag{5.4}$$

The quantities Z_1 and Y_1 are given by

$$Z_1 = i\omega \frac{1}{T_w} \frac{J_0(k_v)}{J_2(k_v)}, \quad Y_1 = -i\omega M^2 \left[\gamma + (\gamma - 1) \frac{J_2(k_t)}{J_0(k_t)} \right], \quad (5.5)$$

as stated in Fedorov *et al.* (2001). Here, J_0 and J_2 are Bessel functions of the first kind and T_w is the wall-surface temperature, which is $T_w = 1$ for the considered isothermal case. The arguments k_v and k_t of the Bessel functions read

$$k_v = r \sqrt{\frac{i\omega\rho_w}{\mu_w} Re}, \quad k_t = k_v \sqrt{Pr}, \quad (5.6)$$

with ρ_w and μ_w as the mean density and viscosity at the wall surface. Further, Pr denotes the Prandtl number. The quantities are scaled with the free-stream parameters. Thus, $Re = U_\infty \rho_\infty \delta / \mu_\infty$ is the free-stream Reynolds number. With regard to the dependency of the porous wall admittance (5.3) on the key parameters h and ϕ , it is reasonable that for vanishing porous-layer thickness $h = 0$ or porosity $\phi = 0$, (5.3) yields the admittance $Y = 0$ of rigid walls.

In the context of the inviscid consideration adopted in this paper, we simplify the admittance model for the high-Reynolds-number limit $Re \rightarrow \infty$. Using the asymptotic expansions of the Bessel functions $J_\nu(z)$ for $z \rightarrow \infty$ in case $|\arg(z)| < \pi$, as provided in Bender & Orszag (1999), it can be derived that $\lim_{z \rightarrow \infty} J_0(z)/J_2(z) = -1$ holds. With this, (5.5) simplifies in the inviscid limit to

$$Z_1 = i\omega \frac{1}{T_w}, \quad Y_1 = -i\omega M^2. \quad (5.7)$$

Substituting (5.7) into (5.4) yields for Z_0 and Λ the form

$$Z_0 = \frac{1}{M\sqrt{T_w}}, \quad \Lambda = \text{sign}(\omega_i) \frac{i\omega M}{\sqrt{T_w}}, \quad (5.8)$$

ensuring $\text{Re}(\Lambda) < 0$. Plotting the admittance Y of the viscous model against the admittance Y of our simplified model for the inviscid case reveals that the viscous Y approaches the inviscid limit continuously as k_v is increased, justifying the use of the simplified inviscid model.

We are now interested in the effects of a porous layer on the boundary-layer stability. To this end, we investigate the influence of the porous-layer thickness h and the porosity ϕ on the instability modes. First, in § 5.3.2 we investigate the influence on the 2-D modes in the $M = 4.2$ boundary layer to examine whether the effects we observed for constant admittances Y in § 5.2.1 also hold for porous walls. Subsequently, in § 5.3.3, we also consider 3-D modes. The aim is to investigate the maximum growth with a focus on the maximum growth rate and the corresponding propagation direction under variation of the layer thickness h .

5.3.2. Effects of porous walls on 2-D modes

To study the effects of porous layers on the 2-D instabilities, figure 7 shows the growth rate ω_i of the 2-D modes plotted against the wavenumber α for different porosity ϕ . The results were obtained once for a very large porous-layer thickness $h = 300$ (figure 7a) and once for a very small layer thickness $h = 0.5$ (figure 7b), both at a Mach number of $M = 4.2$. As reference, the curve for the rigid-wall case $\phi = 0$ (black curve) is plotted, which represents the dominant second-mode instability in figure 3(a).

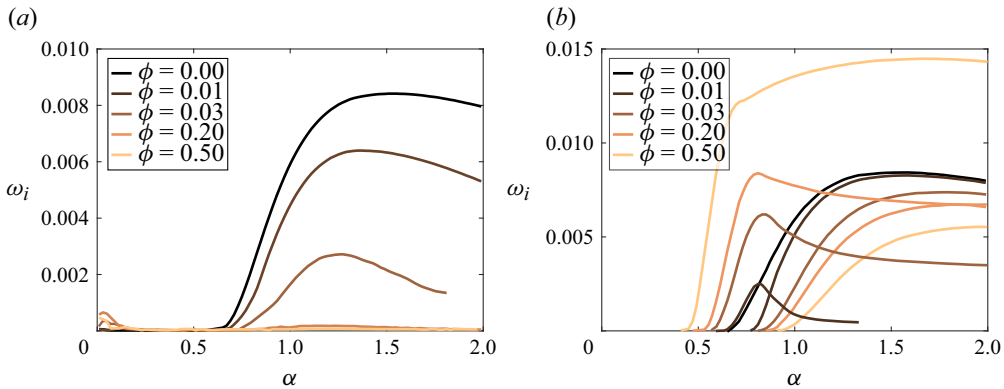


Figure 7. Growth rate ω_i of the 2-D modes plotted against α in the $M = 4.2$ boundary layer for different wall porosities ϕ and two different porous-layer thicknesses h : (a) $h = 300$, (b) $h = 0.5$.

In the following, we first discuss the results for the large layer thickness $h = 300$. Subsequently, we compare them with those for the small layer thickness $h = 0.5$.

Effects for large porous-layer thickness [Figure 7\(a\)](#) reveals that the same effects can be observed for porous walls with large porous-layer thickness h as for constant wall admittance Y in § 5.2. On the one hand, we see that the dominant second-mode instability, which shows significant growth rates in the range of larger wavenumbers α in the rigid-wall case $\phi = 0$, is damped by the thick porous layer for porosities $\phi > 0$, i.e. the growth rates ω_i in the larger α spectrum are reduced for $\phi > 0$. Increasing the wall porosity ϕ leads to a stronger reduction of the second-mode growth rates, until for sufficiently large porosity ϕ quasi-complete stabilisation is achieved in the range of large α , as can be seen here for example for $\phi = 0.5$, where the growth rates for high α are of the order of 10^{-5} . This damping effect on the second mode, up to almost complete stabilisation for large admittances, is consistent with the observations for constant Y in § 5.2.

In addition to the damping effect, however, we also observe a destabilising effect of the porous wall. Above certain porosities ϕ , here in [figure 7\(a\)](#) for $\phi \geq 0.1$, new pronounced unstable growth rates ω_i occur in the range of smaller α , just as found before for very large constant admittances Y . This new instability at small α is a first mode, as already observed for constant admittances Y . The corresponding eigenfunction is shown in [Appendix A](#). This first-mode instability becomes more unstable with an increase in porosity ϕ up to a certain value. However, for all ϕ , its growth rates are well below the maximum growth rate of the second mode in the rigid-wall case.

The aforementioned effects, observed in [figure 7\(a\)](#) for the thick porous layer, are qualitatively consistent with previous literature. Fedorov *et al.* (2003), for example, also found for boundary layers with porous coating a strong stabilisation of the second mode, dominant in the range of high frequencies, and a slight destabilisation of the first mode at low frequencies.

Effects for small porous-layer thickness If we look at [figure 7\(b\)](#), we see that walls with a very small porous-layer thickness h also lead to a damping of the second mode at large wavenumbers α , i.e. there is also a reduction in the second-mode growth rate for porosities $\phi > 0$ compared with the rigid-wall case $\phi = 0$ (black curve). In comparison with the damping effect resulting from the large layer thickness in [figure 7\(a\)](#), however, the second-mode damping is significantly weaker for the small layer thickness $h = 0.5$ here in [figure 7\(b\)](#) and complete stabilisation is not achieved, even for high porosity ϕ .

Apart from this damping effect, we also observe the occurrence of a new instability for the small porous-layer thickness h in [figure 7\(b\)](#). However, this destabilisation resulting from the thin porous layer differs significantly from the destabilisation resulting from thick layers, both in terms of the wavenumber spectrum α , where the destabilisation takes place, and in terms of the magnitude of the growth rates ω_i of the excited modes. As can be seen from [figure 7\(b\)](#), for very small porosity (here, for example, for $\phi = 0.01$), the new instability occurs primarily in an α range around a peak (here around $\alpha \approx 0.8$), coinciding with the range of the smallest wavenumbers, where the second mode in the rigid-wall case becomes relevant. With increasing ϕ , the wavenumber range of the excited instability expands to larger α . At the same time, its growth rates increase significantly. With regard to the increase in the growth rates for increasing ϕ , we observe two things. Firstly, we see that there is a critical value of porosity, here slightly greater than $\phi = 0.1$, above which the excited mode shows a larger maximum growth rate than the damped second mode at its peak. Secondly, for even higher ϕ , as here for $\phi = 0.5$, the growth rates of the new instability become considerably more unstable than the growth rates of rigid-wall second mode (black curve) over the entire α range. At the same time, there is no longer a pronounced peak with respect to ω_i . Instead, the maximum growth rate shifts towards larger wavenumbers. This result of the occurrence of instabilities for very thin porous layers with high porosity, which are significantly more unstable than the dominant mode in the rigid-wall case, is quite central.

The eigenfunction of the destabilised mode given in [Appendix A](#) suggests that it is a second mode, which is consistent with it occurring at large wavenumbers α . This implies that porous walls with very small layer thickness h lead to the destabilisation of a different type of mode from that observed for large porous-layer thickness h or in the literature where, as discussed above, the destabilisation manifests itself in the form of the first mode while the second mode is stabilised.

5.3.3. Influence of porous-layer thickness on maximum growth of 3-D modes

As we saw in the previous section, for walls with sufficiently high porosity ϕ , the dominant growth is no longer given by the original second mode, but by a mode that is destabilised by the porous wall. Both the wavenumbers where this excited instability is relevant and its character, i.e. whether it is a first or second mode, depend strongly on the porous-layer thickness h , while the porosity ϕ mainly determines the strength of the stabilising and destabilising effects. However, the results in the previous section were limited to 2-D modes. We therefore now extend the investigations to 3-D modes. The focus is on the propagation direction of the maximum growth of the excited mode and on its maximum growth rate itself. We want to answer the question of how these change with variation of the layer thickness.

For this purpose, [figure 8](#) shows, on the one hand, the maximum growth rate $\omega_{i,\max}$, occurring over all wavenumbers α and β (see [figure 8\(a\)](#)), and, on the other hand, the corresponding direction of propagation $\gamma = \arctan(\beta/\alpha)$ of this maximum growth (see [figure 8\(b\)](#)), each plotted over the layer thickness h .

Additionally, the corresponding wavenumbers α and β , at which the maximum growth rate occurs, are shown in [figure 8\(b\)](#). The results were obtained for Mach number $M = 4.2$ at a relatively high porosity of $\phi = 0.5$, ensuring that the dominant growth rates are given by the excited mode for layer thicknesses $h > 0$. The curve for $h = 0$ correspond to the maximum growth of the second mode in the rigid-wall case.

Influence on the maximum growth rate If we now consider [figure 8\(a\)](#) for the maximum growth rate $\omega_{i,\max}$, we observe in the range of thin porous layers h that the maximum growth rate increases steeply with increasing h . This suggests the conclusion that thin

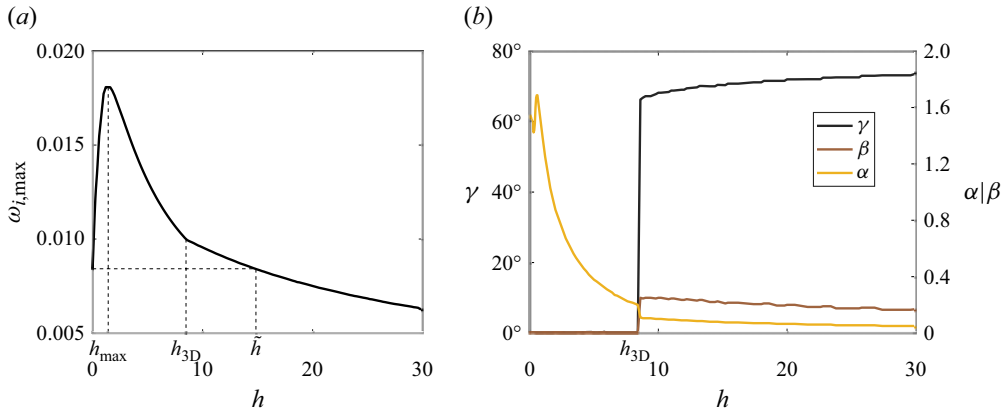


Figure 8. (a) Maximum growth rate $\omega_{i,max}$ and (b) corresponding direction of propagation γ and wavenumbers α , β of the maximum growth plotted against the porous-layer thickness h for $M = 4.2$ and wall porosity $\phi = 0.5$.

porous layers can induce growth rates that are higher than the maximum second-mode growth rates in the rigid-wall case $h = 0$. The occurrence of growth rates greater than that for the rigid wall has already been observed in figure 7(b) for small thickness $h = 0.5$.

Figure 8(a) shows that $\omega_{i,max}$ increases up to a layer thickness marked by h_{max} . For $h > h_{max}$, an increase in h leads to a successive reduction in the maximum growth rate, whereby above a layer thickness \tilde{h} damping is achieved compared with the dominant rigid-wall instability. This effect of reducing the maximum growth rate by thick porous layers has already been seen in figure 7(b), where the destabilised first mode shows significantly lower growth rates than the rigid-wall second mode.

Influence on the direction of maximum growth To answer the question regarding the influence of the layer thickness h on the direction of propagation of the maximum growth, we consider figure 8(b) showing the propagation angle γ of $\omega_{i,max}$ over h .

Most importantly, the figure reveals that the porous-layer thickness h is a decisive factor in determining whether maximum growth occurs in the 2-D or 3-D direction. For porous layers h above a threshold value h_{3D} the strongest growth occurs in the 3-D direction. This can be attributed to the fact that in these cases $h > h_{3D}$ the amplified instability can be identified as a first mode. The result that the destabilised first mode is most unstable in the 3-D direction is consistent with the results for constant large admittances in § 5.2 as well as with earlier literature on porous walls, such as Fedorov *et al.* (2003). More specifically, figure 8(b) indicates that the 3-D angle of the maximum growth of the first mode remains almost the same for all layer thicknesses $h > h_{3D}$, only increasing marginally with h .

In comparison with the behaviour for $h > h_{3D}$, on the other hand, it is observed that in the range of smaller porous-wall-layer thicknesses $h < h_{3D}$, the dominant instability propagates in the 2-D direction. This 2-D character supports the previous interpretation that the mode induced by a very thin porous layer is a second mode, as discussed in the context of figure 7(b).

For layers $h_{max} < h < h_{3D}$, the eigenfunction of the destabilised mode can be interpreted as a first mode (see Appendix A), despite its 2-D character. However, it should be noted that the characterisation of the eigenfunction is to be discussed.

Comparing figures 8(a) and 8(b), we observe another effect. Relative to the dominant instability for rigid walls $h = 0$, all destabilised 2-D modes are more unstable, while all destabilised 3-D modes with $h > \tilde{h}$ are less unstable than the rigid-wall instability.

However, for the parameters considered here, 3-D instabilities with growth rates greater than in the rigid-wall case can be observed in a narrow range of mean layer thicknesses $h_{3D} < h < \tilde{h}$.

Influence on the wavenumbers Regarding the wavenumbers, [figure 8\(b\)](#) reveals that, apart from the range of very small h , α decreases with h , which implies that the maximum growth shifts to smaller streamwise wavenumbers as h increases. This is consistent with the results in [figure 7](#), where it was found for high porosity ϕ that in the case of small $h = 0.5$ the strongest instability occurs in the form of the destabilised second mode at high wavenumbers α , while for large $h = 300$ the destabilised first mode at small α is the dominant mode. In the range of 3-D growth, α remains almost constant, decreasing only slightly. Regarding the spanwise wavenumber β of maximum growth, we observe for $h > h_{3D}$ that it occurs around $\beta \approx 0.2$ given the parameters considered. This is consistent with the results for large constant admittances Y in [figure 6](#).

To summarise, three ranges of the porous-layer thickness can be observed with respect to the destabilisation of porous walls with high porosity. Firstly, the range of small layer thicknesses h , where a 2-D instability is induced at high wavenumbers α , leading to growth rates greater than those for rigid walls; secondly, a narrow range of mean layer thicknesses h , where a 3-D mode with growth rates greater than for rigid walls occurs; thirdly, the range of large layer thicknesses h , with the strongest growth occurring in the 3-D direction at small α , which is damped compared with a rigid wall.

6. Conclusion

In this work, we have investigated the influence of metasurfaces such as porous walls, described by the acoustic wall admittance Y , on the temporal linear stability of a supersonic exponential boundary-layer flow. We first examined the effects under constant admittance Y before extending the analyses to a porous wall model. Our investigations show mainly two effects. On the one hand, a stabilising effect is observed in the form of damping of the second mode, being the dominant instability in the rigid-wall case. On the other hand, we observe destabilisation occurring in the form of an instability induced by the wall admittance. The key result in this context is that the type of the destabilised mode is decisively determined by the porous-layer thickness. This implies that the direction of maximum growth and the wavenumber range of destabilisation depend on the layer thickness. The porosity of the wall, in contrast, mainly determines the extent of the stabilising and destabilising effects. An increase in porosity leads both to a stronger damping of the rigid wall's second mode and to larger growth rates of the destabilised mode.

The investigations were motivated by the question of whether porous walls, in addition to destabilising the first mode as found in earlier literature, can also lead to destabilisation of other modes. This also implies the question regarding the type of the further induced instabilities and regarding the direction of propagation of the most unstable growth over porous walls. To answer these points, we considered the PBE for the inviscid normal-mode perturbations in the exponential boundary layer, which was solved exactly in terms of the CHF. This allowed the differential eigenvalue problem for boundary-layer stability with wall admittance to be reduced to an algebraic eigenvalue equation. In order to investigate the effects of porous wall linings on the stability, we implemented a frequency-dependent porous wall model for the wall admittance as proposed by Fedorov *et al.* (2001), which introduces the two central wall parameters of porosity ϕ and porous-layer thickness h .

By asymptotic and numerical analysis of the eigenvalue equation, it is shown that full stabilisation of the second mode can be achieved for constant admittances Y . For

sufficiently large wall admittances Y , however, a new first-mode instability is induced in the range of small wavenumbers α , which proves to be most unstable in the 3-D direction. The critical admittance value for the onset of this instability increases with increasing Mach number. For the porous wall model, we observe at Mach number 4.2 that in the case of large porous-layer thicknesses h , mainly the same effects occur as under constant Y . However, compared with the results for constant admittance, for thick porous layers the induced first-mode instability already occurs at porosities ϕ where the second mode is not yet fully stabilised. In the case of small porous-layer thicknesses h , on the other hand, the stabilising effect is significantly weaker. The most important result, though, is that the destabilisation over thin porous wall layers manifests itself in the form of a newly emerging second-mode instability, which occurs at large wavenumbers α with maximum growth in the 2-D direction. Crucial in this context is the observation that for high porosities ϕ , the induced second mode exceeds the growth rates of the rigid-wall case. Due to the different character of the destabilised mode depending on the layer thickness, it follows that the maximum growth for thick porous layers occurs in the 3-D direction, whereas for thin layers it occurs in the 2-D direction. Interesting in this regard is the finding that for medium layer thicknesses, 3-D instabilities can exist that are more unstable than the rigid-wall second mode.

To summarise, we have shown and quantified the sensitivity of the occurrence and the type of the induced instability mode with respect to the porous wall parameters, which is a crucial result for the design of porous wall linings. With the methods used, based on the exact PBE solution, we have thus succeeded in breaking down the fundamental effects of the wall coatings on the boundary-layer stability. It is the aim of further studies to include additional effects such as the wall temperature in the exact solution in order to expand the picture.

Acknowledgements. The authors thank T. Flint, C. Gonzalez and Prof. S. K. Lele from Stanford University for fruitful discussions and their contribution to the numerical validation of eigenvalues.

Funding. L.D.B. acknowledges funding by the Deutsche Forschungsgemeinschaft (DFG, German Research Foundation): OB 96/55-1-456793479. S.G. acknowledges funding by the DFG: SPP 2410 Hyperbolic Balance Laws in Fluid Mechanics: Complexity, Scales, Randomness (CoScaRa), within the project ‘Approximation Methods for Statistical Conservation Laws of Hyperbolically Dominated Flow’ under project number 526024901. The work of S.G. and L.D.B. was further supported by the Graduate School CE within the Centre for Computational Engineering at Technische Universität Darmstadt.

Declaration of interests. The authors report no conflict of interest.

Appendix A. Eigenfunctions

By deriving the exact solution of the PBE with exponential boundary-layer profile, as presented in § 2, the eigenfunctions of the density perturbations $\hat{\rho}(y)$ could be described analytically according to (2.13) in terms of the CHF.

In order to identify the character of the most unstable disturbances both in the case of a rigid wall and in the cases of porous walls with different porous-layer thicknesses, the respective density eigenfunctions are considered in figure 9, plotted as real part (black line) and imaginary part (brown line) over y . Figure 9(a) gives the eigenfunction for the most unstable rigid-wall perturbation. In contrast, the eigenfunctions in figure 9(b–d) belong to the most unstable mode over a porous wall with porosity $\phi = 0.5$ for three different layer thicknesses $h = 0.5$, $h = 5$ and $h = 300$. In addition, in all the panels the corresponding far-field solution $\hat{\rho}_{ff}$, given by (5.2), is shown, with the real part (black dashed line) and the imaginary part (black dotted line) plotted separately. All results refer to a Mach number of 4.2.

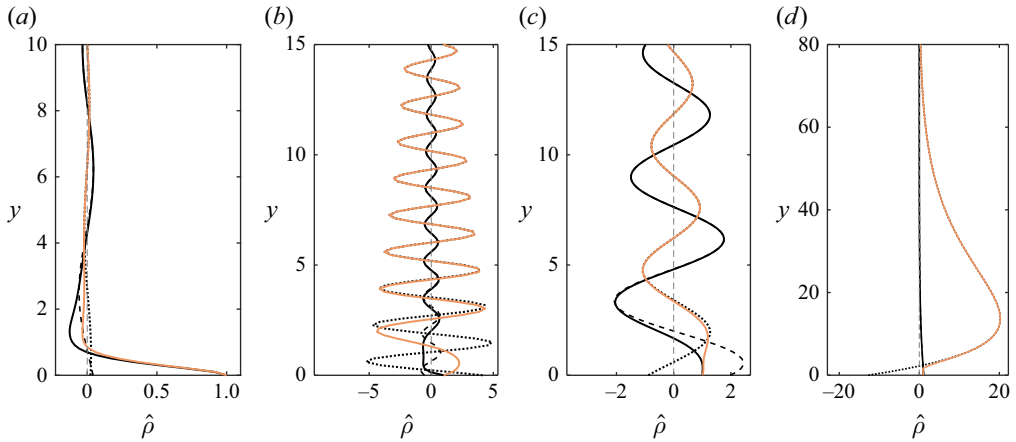


Figure 9. Density eigenfunction $\hat{\rho}$ at wavenumbers α , β of the most unstable eigenvalue for different walls. (a) Rigid wall; and porous walls with porosity $\phi=0.5$ and layer thickness (b) $h=0.5$, (c) $h=5$ and (d) $h=300$. Real part (black line) and imaginary part (brown line) are plotted separately. Further, the real part (black dashed line) and imaginary part (black dotted line) of the far-field solution are shown. (a) rigid wall: $\alpha = 1.55$, $\beta = 0$; (b) $h = 0.5$: $\alpha = 1.67$, $\beta = 0$; (c) $h = 5$: $\alpha = 0.38$, $\beta = 0$; (d) $h = 300$: $\alpha = 0.04$, $\beta = 0.13$.

As can be seen from figure 9(a), the eigenfunction $\hat{\rho}$ of the most unstable perturbation over the rigid wall has one zero crossing when subtracting the far-field oscillations $\hat{\rho}_{ff}$, which characterises it as a second mode, consistent with it being most unstable in the 2-D direction, as discussed in § 5.2.3. The same is true for the most unstable disturbance at the small porous-layer thickness $h = 0.5$ (see figure 9b), which also has 2-D character. In contrast, the most unstable perturbation for large $h = 300$ proves to be a first mode corresponding to its 3-D character, as the eigenfunction in figure 9(d) has no zero crossing apart from the far-field oscillation. The eigenfunction at $h = 5$ in figure 9(c) suggests that this is also a first mode, despite its 2-D character.

From $\hat{\rho}(y)$, the velocity eigenfunctions $\hat{u}(y)$ and $\hat{v}(y)$ are obtained from the decoupled linearised Euler equations with the normal-mode approach. In the case of 2-D perturbations, this yields

$$\hat{u} = -\frac{dU_0}{dy} \frac{1}{M^2(\omega - U_0\alpha)^2} \frac{d\hat{\rho}}{dy} + \frac{\alpha}{M^2(\omega - U_0\alpha)} \hat{\rho}, \quad (\text{A1})$$

$$\hat{v} = -\frac{i}{M^2(\omega - U_0\alpha)} \frac{d\hat{\rho}}{dy}. \quad (\text{A2})$$

Appendix B. Symmetries of solutions of the eigenvalue problem

It is of interest to find out if there exist transformations

$$(\tilde{\alpha}, \tilde{\omega}, \tilde{\hat{\rho}}) = \mathbf{f}(\alpha, \omega, \hat{\rho}) \quad (\text{B1})$$

that allow one to determine new solutions $(\tilde{\alpha}, \tilde{\omega}, \tilde{\hat{\rho}})$ of the eigenvalue problem from other given solutions $(\alpha, \omega, \hat{\rho})$. This can deepen the understanding of the stability behaviour. Let

$$\mathbf{D}(\hat{\rho}, \alpha, \omega) = 0 \quad (\text{B2})$$

formally denote the eigenvalue problem consisting of the PBE (2.3) as a differential equation and the two BCs (2.4) and (2.6), which has the solution $(\alpha, \omega, \hat{\rho})$. In order for

the transformed set $(\tilde{\alpha}, \tilde{\omega}, \tilde{\rho})$ to also form a solution of (B2), we have to require

$$\mathbf{D}(\tilde{\rho}, \tilde{\alpha}, \tilde{\omega}) = 0. \tag{B3}$$

Equation (B3) is exactly the case if the transformation (B1) leaves both the PBE and the BCs form invariant. In this case, the transformation (B1) is called the equivalence transformation of the eigenvalue problem, providing further solutions to be obtained from given ones $(\alpha, \omega, \hat{\rho})$. The term equivalence transformations refers to a special class of symmetry transformations involving the transformation of parameters. In the following, we therefore simply speak of symmetry transformations or symmetries. For detailed literature on the symmetry idea, the reader is referred to Bluman & Anco (2002).

Regarding the stability analysis, especially those symmetry transformations that couple stable eigenvalues with unstable eigenvalues are of central importance. This is particularly relevant in view of the objective of boundary-layer stabilisation by means of impedance walls. We therefore discuss in the following the two underlying symmetries of our eigenvalue problem, which involve complex conjugation and reflection of the eigenvalues, thus leading to such a stable–unstable coupling. We will see that the impedance BC plays a decisive role in this regard.

B.1. Symmetry regarding complex conjugation

We start with investigating the equations with respect to complex conjugation, meaning that we consider the transformation

$$(\tilde{\alpha}, \tilde{\omega}, \tilde{\rho}) = (\alpha, \omega^*, \hat{\rho}^*), \tag{B4}$$

in which the eigenvalues and eigenfunctions are subjected to complex conjugation with the real wavenumber α unchanged. To see whether the eigenvalue problem is form invariant under (B4), we carry out complex conjugation of the PBE (2.3) and the BCs (2.4) and (2.6). Applying the rules for complex conjugation, the PBE yields

$$\frac{d^2 \hat{\rho}^*}{dy^2} + \frac{2\alpha}{\omega^* - U_0\alpha} \frac{dU_0}{dy} \frac{d\hat{\rho}^*}{dy} + \left[M^2(\omega^* - U_0\alpha)^2 - \alpha^2 \right] \hat{\rho}^* = 0. \tag{B5}$$

We see that (B5) provides an equation form invariant to the initial PBE (2.3). The same holds for the far-field condition (2.4) after complex conjugation.

For the impedance BC, however, this is not guaranteed. Complex conjugation of (2.6) yields

$$\left. \frac{d\hat{\rho}^*}{dy} \right|_{y=0} = i \omega^* (Y(\omega))^* \hat{\rho}^*(0). \tag{B6}$$

Comparing (B6) with (2.6) reveals that the impedance BC for the complex conjugated solution $(\alpha, \omega^*, \hat{\rho}^*)$ differs from the initial impedance condition for the solution $(\alpha, \omega, \hat{\rho})$ in terms of both the sign on the right-hand side and the admittance occurring in complex conjugated form in (B6). Consequently, the impedance condition is in general not form invariant with respect to the complex conjugation (B4), which means that for general wall admittances $Y(\omega)$ the eigenvalues do not occur in a complex conjugate manner.

However, there are two exceptions in which form invariance of the impedance condition is given. The first is the case of a rigid wall, where $Y = 0$ causes the right-hand sides of (2.6) and (B6) to vanish, thus leading to form invariance. Consequently, for rigid walls, (B4) represents a symmetry of the eigenvalue problem, implying that for every stable

eigenvalue ω also the complex conjugate unstable eigenvalue ω^* occurs. In the case of non-rigid walls, on the other hand, form invariance between the complex conjugate impedance condition (B6) and the original form (2.6) persists only for impedance models that fulfil

$$Y^*(\omega) = -Y(\omega^*). \tag{B7}$$

In order for (B7) to be compatible with the reality condition, reading $Y^*(\omega) = Y(-\omega)$ for $\omega \in \mathbb{R}$, and the condition of passivity, reading $\text{Re}(Y(\omega)) \geq 0$ for $\omega \in \mathbb{R}$, formulated in Rienstra (2006) as fundamental conditions for physical impedance models, the following must hold:

$$Y_r(\omega) = 0, \quad Y_i(-\omega) = -Y_i(\omega) \quad \text{for } \omega \in \mathbb{R}. \tag{B8}$$

Thus, admittances $Y(\omega)$, which fulfil (B7) and (B8), form the second exception, under which the impedance BC is invariant with respect to (B4) and for which there is therefore a coupling of stable and unstable solutions due to the complex conjugation, as in the case of rigid walls.

To interpret the condition (B7), we note that it reads $Y_r(\omega) - iY_i(\omega) = -Y_r(\omega^*) - iY_i(\omega^*)$ when written out, which means that the admittances associated with the two complex conjugate stable and unstable eigenvalues ω and ω^* result from each other by reflection of the admittance real part. This is consistent with the fact that for quiescent fluids it can be shown that the sign of the real part of the wall impedance determines whether the wall acts as a source of energy absorption or energy production (see Rienstra & Hirschberg 2001), thereby causing stabilisation or destabilisation.

B.2 Reflection symmetry

Similarly as under the previously discussed complex conjugation, the eigenvalue problem also behaves under reflection of α and ω . So we consider the transformation

$$(\tilde{\alpha}, \tilde{\omega}, \tilde{\rho}) = (-\alpha, -\omega, \rho). \tag{B9}$$

Applying (B9) to the PBE (2.3) and the far-field condition (2.4) reveals them to be form invariant under this reflection of α and ω .

The impedance BC (2.6), on the other hand, is transformed by (B9) to

$$\left. \frac{d\tilde{\rho}}{dy} \right|_{y=0} = i \tilde{\omega} Y(-\tilde{\omega}) \tilde{\rho}(0), \tag{B10}$$

which differs from the impedance condition (2.6) in terms of the sign on the right-hand side as well as the sign in the argument of the admittance model $Y(\omega)$, thus breaking the symmetry for general admittances.

An exception is again the case of a rigid wall $Y = 0$. A further exception are impedance models, which comply with

$$Y(-\omega) = -Y(\omega), \tag{B11}$$

causing the transformed and original impedance BCs (B10) and (2.6) to be invariant in form. Compatibility of (B11) with the reality and passivity condition of Rienstra (2006) also requires

$$Y_r(\omega) = 0 \quad \text{for } \omega \in \mathbb{R}. \tag{B12}$$

In these two exceptional cases, the case of $Y = 0$ or impedance models $Y(\omega)$ fulfilling (B11) and (B12), (B9) is a symmetry of the eigenvalue problem, which implies that for

each eigenvalue pair (α, ω) , there also exists the reflected eigenvalue pair $(-\alpha, -\omega)$ with the same phase velocity but opposite stability behaviour. For other impedances, however, which do not comply with these conditions, this stable–unstable coupling of the reflected eigenvalues is no longer present.

It should be noted that for constant real admittances $Y \in \mathbb{R}$, being consistent with the fundamental conditions of Rienstra (2006), form invariance of the impedance conditions (2.6) and (B10) can be achieved by extending the transformation (B9) by a reflection of the admittance, namely

$$(\tilde{\alpha}, \tilde{\omega}, \tilde{\rho}, \tilde{Y}) = (-\alpha, -\omega, \hat{\rho}, -Y). \tag{B13}$$

Equation (B13) thus represents a symmetry of the problem under the assumption of constant real Y . From this it can be concluded that reflection of Y transfers the solutions $(\alpha, \omega, \hat{\rho})$ into solutions $(-\alpha, -\omega, \hat{\rho})$ having opposite stability behaviour, corresponding to the fact that the sign of the admittance real part determines whether energy is absorbed or produced (Rienstra & Hirschberg 2001).

B.3 Symmetry of the combination of complex conjugation and reflection

Combining the transformation of complex conjugation (B4) and of reflection (B9) yields

$$(\tilde{\alpha}, \tilde{\omega}, \tilde{\rho}) = (-\alpha, -\omega^*, \hat{\rho}^*). \tag{B14}$$

Just like the two transformations themselves, their combination (B14) also leaves the PBE (2.3) and the far-field BC (2.4) invariant in terms of their form. Applying (B14) to the impedance BC (2.6), however, yields, after complex conjugation, the form

$$\left. \frac{d\tilde{\rho}}{dy} \right|_{y=0} = -i \tilde{\omega} Y^* (-\tilde{\omega}^*) \tilde{\rho}(0). \tag{B15}$$

The latter is only form invariant to (2.6) for $Y = 0$ or constant real $Y \in \mathbb{R}$ as well as for models $Y(\omega)$ satisfying the relation

$$Y(\omega) = Y^*(-\omega^*), \tag{B16}$$

which is equivalent to the reality condition in Rienstra (2006) for $\omega \in \mathbb{R}$. In these three cases of a rigid wall, real constant Y or admittances $Y(\omega)$ with (B16), the the combination of reflection and complex conjugation (B14) represents a symmetry of the problem, implying that the solutions $(\alpha, \omega, \hat{\rho})$ and $(-\alpha, -\omega^*, \hat{\rho}^*)$ occur together. Due to $-\omega^* = -\omega_r + i \omega_i$, the eigenvalues (α, ω) and $(-\alpha, -\omega^*)$ have the same stability behaviour and phase velocity, which means that in these three cases of Y , the same stability effects can be observed for positive and negative wavenumbers α .

Appendix C. Solution of the PBE for an exponential shear profile

For the PBE with the exponential boundary-layer profile, Zhang & Oberlack (2021) found an analytical solution in terms of the CHF. An equivalent form of this solution is derived in the following. The procedure for this is based on transforming the PBE (2.8) including the BL profile into the CHE. As the PBE results from an inviscid consideration, it is subject to singularities like all inviscid equations. In general, the singularities of ODEs determine the character of the solutions and are therefore crucial for finding a solution. We thus analyse the PBE with respect to the singularities of its coefficient functions. For this, we transfer the PBE (2.8) from the semi-infinite domain $y \in [0, \infty)$ to the finite domain

$z \in [0, \alpha/(\alpha - \omega)]$ by the transformation

$$z = \frac{\alpha}{\alpha - \omega} e^{-y}, \tag{C1}$$

which simplifies the analysis of singularities. Equation (C1) matches the far field to the point $z = 0$ and the wall to $z = \alpha/(\alpha - \omega)$. Applying the transformation (C1) to (2.8) provides

$$\frac{d^2 \hat{\rho}}{dz^2} - \frac{z + 1}{z(z - 1)} \frac{d\hat{\rho}}{dz} + \frac{M^2(\alpha - \omega)^2(z - 1)^2 - \alpha^2}{z^2} \hat{\rho}(z) = 0. \tag{C2}$$

The singularities of the coefficient functions in the latter ODE can be read off, yielding

$$z_s = \{0, 1, \infty\}. \tag{C3}$$

Here, the far field at $z_s = 0$ as well as $z_s = 1$ are regular singular points and $z_s \rightarrow \infty$ is an irregular singular point. For details of singularities of ODEs, the reader is referred to Olver *et al.* (2010). From (C1), the regular singularity $z = 1$ can be identified as the critical layer, describing the point where $U_0 = \omega/\alpha$, i.e. where the phase velocity of the perturbation equals the mean flow velocity. Special properties of this critical-layer singularity for the exponential boundary layer are discussed in Zhang *et al.* (2022).

As stated by Ronveaux & Arscott (1995), an ODE with one irregular and two regular singularities is reducible by suitable transformations to the standard form of the confluent Heun equation:

$$\frac{d^2 w}{dz^2} + \left(\epsilon + \frac{\gamma}{z} + \frac{\delta_H}{z - 1} \right) \left(\frac{dw}{dz} \right) + \frac{(\alpha_H z - q)}{z(z - 1)} w(z) = 0, \tag{C4}$$

having exactly the same singularities as (C2). Note that the subscript H is used to distinguish the Heun parameters from the physical quantities. In order to reduce (C2) to the CHE form (C4), we carry out a transformation of the dependent variable $\hat{\rho}(z) \rightarrow w(z)$ given by

$$w(z) = \hat{\rho}(z) e^{iMz(\omega - \alpha)} \left(\frac{z(\alpha - \omega)}{\alpha} \right)^{\sqrt{\theta}}, \tag{C5}$$

which results from applying the methods of Ronveaux & Arscott (1995) to our problem. Here, we introduced the complex far-field wavenumber as an abbreviation according to

$$\sqrt{\theta} = \sqrt{\alpha^2 - M^2(\omega - \alpha)^2}. \tag{C6}$$

With the transformations (C1) and (C5), the PBE (2.8) can finally be converted to an ODE in the form of the CHE (C4), where the coefficients are read off as

$$\begin{aligned} q &= iM(\alpha - \omega) - 2M^2(\alpha - \omega)^2 - 2\sqrt{\theta}(iM(\alpha - \omega) + 1), \\ \alpha_H &= -M(\alpha - \omega) \left(2M(\alpha - \omega) + i \left(2\sqrt{\theta} + 1 \right) \right), \\ \gamma &= -2\sqrt{\theta} + 1, \quad \delta_H = -2, \quad \epsilon = 2iM(\alpha - \omega). \end{aligned} \tag{C7}$$

This allows the PBE (2.8) to be solved in terms of the CHF as the solution of the CHE, with the coefficients (C7) specifying the solution of (2.8).

Transforming the solution for $w(z)$ back to the initial set of variables $\hat{\rho}(y)$ yields the general solution of the PBE for the exponential profile, given by (2.9). Therein,

HeunC_{1/2}(; z) are the basic power series representations with root 0 of the two solution branches around z = 0. They can be transferred to an equivalent form around the other regular singular points.

In order to evaluate the CHF occurring in the PBE solution, the Matlab implementation by Motygin (2018), used in this work, is based on the two linearly independent solution branches of the CHE as power series around the respective singularity. Their radii of convergence are up to the nearest singularity. Further, Motygin implemented analytic continuation of the power series outside their radii of convergence, with the benefit of evaluating the CHF at points outside the power series' radii of convergence. This implementation has a branch cut on the negative real z axis, excluding these values from the consideration. However, since we are especially interested in stable or unstable eigenvalues with ω_i ≠ 0, the CHF is always evaluated above or below the real axis and thus outside the branch cut.

Appendix D. Asymptotic analysis for small α

D.1 Procedure of the asymptotic analysis for small α

The basis of the asymptotic analysis for small wavenumbers α is the power series expansion (4.1) of the solutions ω in the small parameter α. In order to determine the constant coefficients a_m, m = 1, 2, . . . , n, in this series approach, so that it forms a good approximation of the eigenvalues ω at small α, (4.1) is inserted into the eigenvalue equation (2.14). All terms of the equation are subsequently developed as a series in α. The latter step necessitates a power series expansion of the CHF in (2.14). For |z| < 1, this Heun function, describing the selected $\hat{\rho}$ solution branch (2.13), can be represented as the power series (Ronveaux & Arscott 1995)

$$\text{HeunC}_2(q, \alpha_H, \gamma, \delta_H, \epsilon, z) = \sum_{k=0}^{\infty} c_k z^k. \tag{D1}$$

The coefficients c_n in (D1) are obtained via recursion formulas as functions of the coefficients of our Heun function, starting with c₀ = 1. This gives the first terms of the Heun series (D1) as

$$\text{HeunC}_2(q, \alpha_H, \gamma, \delta_H, \epsilon, z) = \sum_{k=0}^{\infty} c_k z^k = 1 + \frac{\delta_H - \epsilon - \gamma + (1 - \delta_H + \epsilon)\gamma - q}{2 - \gamma} z + O(z^2). \tag{D2}$$

Deriving (D2) with respect to the argument z yields the power series for HeunC₂' in (2.14).

After expressing all terms in the eigenvalue equation (2.14) by power expansions in α and subsequently collecting the coefficients of the powers of α, the eigenvalue equation can be written in the form

$$f_1(a_1; M, Y) \alpha + f_2(a_1, a_2; M, Y) \alpha^2 + \dots + f_n(a_1, \dots, a_n; M, Y) \alpha^n + O(\alpha^{n+1}) = 0, \tag{D3}$$

where f_m(a₁, . . . a_m; M, Y) are algebraic expressions for the constants a_m of (4.1). For (D3) to be valid for any α, each term in (D3) must vanish separately, meaning

$$f_m(a_1, \dots, a_m; M, Y) = 0 \quad \text{for } m = 1, 2, \dots \tag{D4}$$

Equation (D4) thus provides algebraic equations for the coefficients a_1, \dots, a_n as functions of the parameters M and Y . Inserting the solutions a_1 to a_n back into the asymptotic power series approach (4.1) finally yields approximations for the eigenvalues ω at small α up to the order $\mathcal{O}(\alpha^{n+1})$.

D.2 Convergence of the series of the CHF

To assess the validity of the asymptotic eigenvalue solutions (4.1) for small α , it is crucial to examine the convergence of the series expansion (D2). The latter describes the CHF in the chosen solution branch (2.13) expressed as a power series around $z = 0$, whereby due to the transformation (C1) $z = 0$ describes the far field $y \rightarrow \infty$. Because of the appropriate choice of the solution branch, as described in § 2, it is ensured that the solution (2.13) fulfils the far-field BC (2.4).

In order for the asymptotic method to be valid for our boundary-layer problem, it is necessary that the convergence of the Heun series (D2) covers the entire physical region of the boundary-layer flow. This means that the whole area between the far-field condition at $z = 0$ and the impedance BC (2.6) at the wall $z_w = (\alpha)/(\alpha - \omega)$, where the solution $\hat{\rho}$ is evaluated, thus giving the eigenvalue equation, must lie within the convergence radius of the Heun series. As stated in Ronveaux & Arscott (1995), the convergence of the Heun series (D1) is restricted to $|z| < 1$. Accordingly, the Heun series only converges on the entire area between the far field and the wall if $|z_w| < 1$. This implies that the asymptotic expansion is just valid for eigenvalues $\omega(\alpha)$ with $|(\alpha)/(\alpha - \omega)| < 1$. For the other asymptotic results with $|(\alpha)/(\alpha - \omega)| > 1$, it is only ensured that, on the one hand, the series solution for $\hat{\rho}$ is exact within the convergence radius, and, on the other hand, the eigenvalue equation, and consequently the impedance wall BC, is fulfilled up to the order $\mathcal{O}(\alpha^{n+1})$, as the coefficients a_n have been determined accordingly. In order for these results with $|(\alpha)/(\alpha - \omega)| > 1$ to still represent good eigenvalue approximations, it is necessary that the leading terms of the series (D2) approximate the behaviour of the Heun function sufficiently well even beyond the edge of the convergence radius up to the wall. Against this background, it must be kept in mind that asymptotic results for which $|z_w| > 1$ applies can serve as indications for eigenvalues from which conclusions can be drawn about the stability behaviour. However, validation with numerical results is necessary.

Validating the asymptotic eigenvalues with eigenvalues from numerics is also advisable, since in practice when determining the asymptotic solutions (4.1) only the terms up to a certain power α^n are taken into account. The neglect of the higher-order terms is justified due to the consideration of small α ; however, it can lead to inaccuracies if the Heun series shows alternating convergence behaviour.

Appendix E. Scaling of the eigenvalues

As pointed out in § 5.2.1, our results differ from those of previous experimental studies with respect to the wavenumber α , at which we observe maximum growth of the second mode in the rigid-wall case. Due to this, we are interested in whether scaling of the eigenvalues leads to a further set of eigenvalues.

To this end, we consider the transformation

$$\left(\tilde{\alpha}, \tilde{\omega}, \tilde{\rho} \right) = \left(\frac{1}{c}\alpha, \frac{1}{c}\omega, c^2\hat{\rho} \right) \quad \text{with} \quad c \in \mathbb{R}^+, \tag{E1}$$

which scales the eigenvalues and eigenfunctions. Applying (E1) to the PBE (2.3) and the BCs (2.4) and (2.6) provides

$$\frac{1}{c^2} \frac{d^2 \tilde{\rho}}{dy^2} + \frac{2\tilde{\alpha}}{\tilde{\omega} - U_0(y) \tilde{\alpha}} \frac{dU_0(y)}{dy} \frac{1}{c^2} \frac{d\tilde{\rho}}{dy} + \left[M^2 (\tilde{\omega} - U_0(y) \tilde{\alpha})^2 - \tilde{\alpha}^2 \right] \tilde{\rho} = 0, \quad (\text{E2a})$$

$$\lim_{y \rightarrow \infty} \tilde{\rho}(y) = 0, \quad (\text{E2b})$$

$$\left. \frac{1}{c^2} \frac{d\tilde{\rho}}{dy} \right|_{y=0} = -\frac{i}{c} \tilde{\omega} Y(c \tilde{\omega}) \tilde{\rho}(0). \quad (\text{E2c})$$

Since we want to consider scaling of the eigenvalues under unchanged wall admittance, (E2c) generally requires restriction to constant admittances Y .

We now aim to convert equations (E2) for the scaled eigenvalue and eigenfunction into a form similar to the initial PBE (2.3) and BCs (2.4) and (2.6). For this purpose, we scale the wall-normal coordinate

$$\tilde{y} = cy. \quad (\text{E3})$$

With (E3), equations (E2) become

$$\frac{d^2 \tilde{\rho}}{d\tilde{y}^2} + \frac{2\tilde{\alpha}}{\tilde{\omega} - U_0(\tilde{y}/c) \tilde{\alpha}} \frac{dU_0(\tilde{y}/c)}{d\tilde{y}} \frac{d\tilde{\rho}}{d\tilde{y}} + \left[M^2 (\tilde{\omega} - U_0(\tilde{y}/c) \tilde{\alpha})^2 - \tilde{\alpha}^2 \right] \tilde{\rho} = 0, \quad (\text{E4a})$$

$$\lim_{\tilde{y} \rightarrow \infty} \tilde{\rho}(\tilde{y}) = 0, \quad (\text{E4b})$$

$$\left. \frac{d\tilde{\rho}}{d\tilde{y}} \right|_{\tilde{y}=0} = -i \tilde{\omega} Y \tilde{\rho}(0). \quad (\text{E4c})$$

Note that $U_0(\tilde{y}/c)$ corresponds to the given velocity profile with a scaled decay rate in the direction normal to the wall.

It can be seen that equations (E4) are similar to the PBE (2.3) and BCs (2.4) and (2.6) of the initial problem with constant Y , but having a velocity profile with scaled decay rate. Consequently, the eigenvalues and eigenfunctions scaled according to (E1) represent solutions of the boundary-layer problem with scaled velocity profile $U_0(\tilde{y}/c)$. This explains that when investigating boundary layers with velocity profiles of different decay rates, eigenvalues are found scaled to those presented in this paper.

REFERENCES

- AURÉGAN, Y. & LEROUX, M. 2008 Experimental evidence of an instability over an impedance wall in a duct with flow. *J. Sound Vib.* **317** (3-5), 432–439.
- AURÉGAN, Y., STAROBINSKI, R. & PAGNEUX, V. 2001 Influence of grazing flow and dissipation effects on the acoustic boundary conditions at a lined wall. *J. Acoust. Soc. Am.* **109** (1), 59–64.
- BENADE, A.H. 1968 On the propagation of sound waves in a cylindrical conduit. *J. Acoust. Soc. Am.* **44** (2), 616–623.
- BENDER, C.M. & ORSZAG, S.A. 1999 *Advanced Mathematical Methods for Scientists and Engineers I: Asymptotic Methods and Perturbation Theory*. Springer Science & Business Media.
- BLUMAN, G. & ANCO, S. 2002 *Symmetry and Integration Methods for Differential Equation*. Springer-Verlag.
- BRAMBLEY, E. 2013 Surface modes in sheared boundary layers over impedance linings. *J. Sound Vib.* **332** (16), 3750–3767.
- BRAMBLEY, E. & GABARD, G. 2014 Reflection of an acoustic line source by an impedance surface with uniform flow. *J. Sound Vib.* **333** (21), 5548–5565.

- BRAMBLEY, E. 2011 Acoustic implications of a thin viscous boundary layer over a compliant surface or permeable liner. *J. Fluid Mech.* **678**, 348–378.
- BRAZIER-SMITH, P. & SCOTT, J. 1984 Stability of fluid flow in the presence of a compliant surface. *Wave Motion* **6** (6), 547–560.
- BRÈS, G.A., COLONIUS, T. & FEDOROV, A.V. 2010 Acoustic properties of porous coatings for hypersonic boundary-layer control. *AIAA J.* **48** (2), 267–274.
- CAMPOS, L. & SERRÃO, P. 1998 On the acoustics of an exponential boundary layer. *Phil. Trans. R. Soc. Lond. A: Math. Phys. Engng Sci.* **356** (1746), 2335–2378.
- CRIGHTON, D. 1989 The 1988 rayleigh medal lecture: fluid loading—the interaction between sound and vibration. *J. Sound Vib.* **133** (1), 1–27.
- DANIELS, F.B. 1950 On the propagation of sound waves in a cylindrical conduit. *J. Acoust. Soc. Am.* **22** (5), 563–564.
- DE BROECK, L., GÖRTZ, S., FLINT, T., GONZALEZ, C., OBERLACK, M. & LELE, S. 2022 Temporal stability analysis of high mach number boundary layers over cooled impedance walls. In *Studying Turbulence Using Numerical Simulation Databases - XVIII, Proceedings of the CTR Summer Program, 18*, pp. 391–400. Center for Turbulence Research.
- DELFS, J. 2016 Grundlagen der aeroakustik. Technische Universität Braunschweig. Lecture notes, Institut für Aerodynamik und Strömungstechnik, Abteilung Technische Akustik DLR - Deutsches Zentrum für Luft- und Raumfahrt e.V.
- DEMETRIADES, A. 1974 Hypersonic viscous flow over a slender cone. iii-laminar instability and transition. In *7th Fluid and Plasma Dynamics Conference*, p. 535. American Institute of Aeronautics and Astronautics.
- DICKSON, L. E. 1914 *Elementary Theory of Equations*. John Wiley & Sons, Inc.
- DUNN, D.W. & LIN, C.-C. 1955 On the stability of the laminar boundary layer in a compressible fluid. *J. Aeronaut. Sci.* **22** (7), 455–477.
- FEDOROV, A. 2011 Transition and stability of high-speed boundary layers. *Annu. Rev. Fluid Mech.* **43** (1), 79–95.
- FEDOROV, A., KOZLOV, V., SHIPLYUK, A., MASLOV, A. & MALMUTH, N. 2006 Stability of hypersonic boundary layer on porous wall with regular microstructure. *AIAA J.* **44** (8), 1866–1871.
- FEDOROV, A., SHIPLYUK, A., MASLOV, A., BUROV, E. & MALMUTH, N. 2003 Stabilization of a hypersonic boundary layer using an ultrasonically absorptive coating. *J. Fluid Mech.* **479**, 99–124.
- FEDOROV, A.V. 2015 Prediction and control of laminar-turbulent transition in high-speed boundary-layer flows. *Proc. IUTAM* **14**, 3–14.
- FEDOROV, A.V., MALMUTH, N.D., RASHEED, A. & HORNUNG, H.G. 2001 Stabilization of hypersonic boundary layers by porous coatings. *AIAA J.* **39** (4), 605–610.
- FEDOROV, A.V., SOUDAKOV, V. & LEYVA, I.A. 2014 Stability analysis of high-speed boundary-layer flow with gas injection. In *7th AIAA Theoretical Fluid Mechanics Conference*, p. 2498. American Institute of Aeronautics and Astronautics.
- GOLDSTEIN, M. & RICE, E. 1973 Effect of shear on duct wall impedance. *J. Sound Vib.* **30** (1), 79–84.
- HUERRE, P. & MONKEWITZ, P.A. 1985 Absolute and convective instabilities in free shear layers. *J. Fluid Mech.* **159** (1), 151–168.
- KENDALL, J.M. 1975 Wind tunnel experiments relating to supersonic and hypersonic boundary-layer transition. *AIAA J.* **13** (3), 290–299.
- KIMMEL, R. 2003 Aspects of hypersonic boundary layer transition control. In *41st Aerospace Sciences Meeting and Exhibit*, p. 772. American Institute of Aeronautics and Astronautics.
- KIMMEL, R.L., DEMETRIADES, A. & DONALDSON, J.C. 1996 Space-time correlation measurements in a hypersonic transitional boundary layer. *AIAA J.* **34** (12), 2484–2489.
- LEES, L. & LIN, C.-C. 1946 *Investigation of the Stability of the Laminar Boundary Layer in a Compressible Fluid*. National Advisory Committee for Aeronautics.
- LEES, L. & RESHOTKO, E. 1962 Stability of the compressible laminar boundary layer. *J. Fluid Mech.* **12** (4), 555–590.
- LEYVA, I., JEWELL, J., LAURENCE, S., HORNUNG, H. & SHEPHERD, J. 2009 On the impact of injection schemes on transition in hypersonic boundary layers. In *16th AIAA/DLR/DGLR International Space Planes and Hypersonic Systems and Technologies Conference*, p. 7204. American Institute of Aeronautics and Astronautics.
- LYSENKO, V.I. & MASLOV, A.A. 1984 The effect of cooling on supersonic boundary-layer stability. *J. Fluid Mech.* **147** (1), 39–52.
- MACK, L. 1963 The inviscid stability of the compressible laminar boundary layer. *Space Programs Summary* **37**, 23.

- MACK, L. 1964 The inviscid stability of the compressible laminar boundary layer: Part II. *Space Programs Summary* **4**, 165.
- MACK, L. M. 1969 *Boundary-Layer Stability Theory*. Jet Propulsion Laboratory.
- MACK, L. 1984 *Boundary Layer Stability Theory*. North Atlantic Treaty Organization.
- MACK, L. M. 1987 Review of linear compressible stability theory. In *Stability of Time Dependent and Spatially Varying Flows: Proceedings of the Symposium on the Stability of Time Dependent and Spatially Varying Flows Held August 19-23, 1985 at NASA Langley Research Center, Hampton, Virginia*, pp.164–187. Springer.
- MACK, L. M. 1990 On the inviscid acoustic-mode instability of supersonic shear flows: Part 1: two-dimensional waves. *Theor. Comput. Fluid Dyn.* **2** (2), 97–123.
- MALIK, M., ZANG, T. & BUSHNELL, D. 1990 Boundary layer transition in hypersonic flows. In *2nd International Aerospace Planes Conference*, p. 5232. American Institute of Aeronautics and Astronautics.
- MALIK, M.R. 1989 Prediction and control of transition in supersonic and hypersonic boundary layers. *AIAA J.* **27** (11), 1487–1493.
- MALMUTH, N., FEDOROV, A., SHALAEV, V., COLE, J., HITES, M., WILLIAMS, D. & KHOKHLOV, A. 1998 Problems in high speed flow prediction relevant to control. In *2nd AIAA Theoretical Fluid Mechanics Meeting*, p. 2695. American Institute of Aeronautics and Astronautics.
- MARX, D., AURÉGAN, Y., BAILLIET, H. & VALIÈRE, J.-C. 2010 Piv and ldv evidence of hydrodynamic instability over a liner in a duct with flow. *J. Sound Vib.* **329** (18), 3798–3812.
- MASLOWE, S. 1986 Critical layers in shear flows. *Annu. Rev. Fluid Mech.* **18** (1), 405–432.
- MORKOVIN, M. V. 1994 Transition in open flow systems—a reassessment. *Bull. Am. Phys. Soc.* **39**, 1882.
- MOTYGIN, O.V. 2018 On evaluation of the confluent heun functions. *Days Diff.* **2018**, 223–229.
- OLVER, F.W., LOZIER, D.W., BOISVERT, R.F. & CLARK, C.W. 2010 Algebraic and analytic methods. In *The NIST Handbook of Mathematical Functions* (eds F.W.J. Olver, D.W. Lozier, R.F. Boisvert, & C.W. Clark), pp. 1–39. Cambridge University Press.
- PRIDMORE-BROWN, D. 1958 Sound propagation in a fluid flowing through an attenuating duct. *J. Fluid Mech.* **4** (4), 393–406.
- PRODANOV, E.M. 2022 On the cubic equation with its Siebeck–Marden–Northshield triangle and the quartic equation with its tetrahedron. *J. Comput. Sci.* **73**, 102123.
- RASHEED, A., HORNUNG, H., FEDOROV, A. & MALMUTH, N. 2002 Experiments on passive hypervelocity boundary-layer control using an ultrasonically absorptive surface. *AIAA J.* **40** (3), 481–489.
- REED, H. L., SARIC, W. S. & ARNAL, D. 1996 Linear stability theory applied to boundary layers. *Annu. Rev. Fluid Mech.* **28** (1), 389–428.
- REES, E. 1922 Graphical discussion of the roots of a quartic equation. *Am. Math. Mon.* **29** (2), 51–55.
- RESHOTKO, E. 1976 Boundary layer stability and transition. *Annu. Rev. Fluid Mech.* **8** (1), 311–349.
- RESHOTKO, E. 1991 Hypersonic stability and transition. In *Hypersonic Flows for Reentry Problems* (eds J.-A. Desideri, R. Glowinski, & J. Periaux), pp. 18–34. Springer.
- RESHOTKO, E. 1994 Boundary layer instability, transition and control. In *32nd Aerospace Sciences Meeting and Exhibit*, p. 1. American Institute of Aeronautics and Astronautics.
- RESHOTKO, E. 2006 Transition issues at hypersonic speeds. In *44th AIAA Aerospace Sciences Meeting and Exhibit*, pp. 707–715. American Institute of Aeronautics and Astronautics.
- RIEDINGER, X., LES DIZÈS, S. & MEUNIER, P. 2010 Viscous stability properties of a lamb–seen vortex in a stratified fluid. *J. Fluid Mech.* **645**, 255–278.
- RIENSTRA, S. 2006 Impedance models in time domain, including the extended helmholtz resonator model. In *12th AIAA/CEAS Aeroacoustics Conference (27th AIAA Aeroacoustics Conference)*, p. 2686. American Institute of Aeronautics and Astronautics.
- RIENSTRA, S. & HIRSCHBERG, A. 2001 *An Introduction to Acoustics*. Eindhoven University of Technology.
- RIENSTRA, S. W. 2003 A classification of duct modes based on surface waves. *Wave Motion* **37** (2), 119–135.
- RIENSTRA, S.W. & DARAU, M. 2011 Boundary-layer thickness effects of the hydrodynamic instability along an impedance wall. *J. Fluid Mech.* **671**, 559–573.
- RONVEAUX, A. & ARSCOTT, F. 1995 *Heun's Differential Equations*. Clarendon Press.
- SARIC, W. S. 1994 Physical description of boundary-layer transition: experimental evidence. In *AGARD-R-793* (ed. W.S. Saric), pp. 1-1–1-51.
- SCHMID, P. J. & HENNINGSON, D. S. 2001 Transition to turbulence. In *Stability and Transition in Shear Flows* (eds J.E. Marsden & L. Sirovich), pp. 401–475. Springer New York.
- SCHNEIDER, S. P. 1999 Flight data for boundary-layer transition at hypersonic and supersonic speeds. *J. Spacecr. Rockets* **36** (1), 8–20.
- SCHNEIDER, S. P. 2006 Laminar-turbulent transition on reentry capsules and planetary probes. *J. Spacecr. Rockets* **43** (6), 1153–1173.

- SPURK, J. H. & AKSEL, N. 2019 *Strömungslehre*, 9th edn. Springer Vieweg.
- SQUIRE, H. B. & SOUTHWELL, R. V. 1933 On the stability for three-dimensional disturbances of viscous fluid flow between parallel walls. *Proc. R. Soc. Lond. A: Math. Phys. Charact.* **142** (847), 621–628.
- STETSON, K. & KIMMEL, R. 1993 On the breakdown of a hypersonic laminar boundary layer. In *31st Aerospace Sciences Meeting*, p. 896. American Institute of Aeronautics and Astronautics.
- STINSON, M.R. & CHAMPOUX, Y. 1992 Propagation of sound and the assignment of shape factors in model porous materials having simple pore geometries. *J. Acoust. Soc. Am.* **91** (2), 685–695.
- TIAN, X., LIU, T., WANG, T., ZHU, J. & WEN, C. 2022 Double-layer acoustic metasurface for the suppression of the mack second mode in hypersonic boundary-layer flow. *Phys. Fluids* **34** (7), 074105.
- TIAN, X. & WEN, C. 2021 Growth mechanisms of second-mode instability in hypersonic boundary layers. *J. Fluid Mech.* **908**, R4.
- TIAN, X., ZHAO, R., LONG, T. & WEN, C. 2019 Reverse design of ultrasonic absorptive coating for the stabilization of mack modes. *AIAA J.* **57** (6), 2264–2269.
- WAGNER, A., KUHN, M., MARTINEZ SCHRAMM, J. & HANNEMANN, K. 2013 Experiments on passive hypersonic boundary layer control using ultrasonically absorptive carbon–carbon material with random microstructure. *Exp. Fluids* **54** (10), 1–10.
- WAGNER, A., WARTEMANN, V., KUHN, M., DITTERT, C. & HANNEMANN, K. 2015 The potential of ultrasonically absorptive tps materials for hypersonic vehicles. In *20th AIAA International Space Planes and Hypersonic Systems and Technologies Conference*, p. 3576. American Institute of Aeronautics and Astronautics.
- WARTEMANN, V., LÜDEKE, H. & SANDHAM, N. 2009 Stability analysis of hypersonic boundary layer flow over microporous surfaces. In *16th AIAA/DLR/DGLR International Space Planes and Hypersonic Systems and Technologies Conference*, p. 7202. American Institute of Aeronautics and Astronautics.
- WHITEHEAD, A. 1989 NASP aerodynamics. In *National Aerospace Plane Conference. Reston, Virginia: AIAA Paper*, pp. 338–347. American Institute of Aeronautics and Astronautics.
- ZHANG, Y., GÖRTZ, S. & OBERLACK, M. 2022 Over-reflection of acoustic waves by supersonic exponential boundary layer flows. *J. Fluid Mech.* **945**, A9.
- ZHANG, Y. & OBERLACK, M. 2021 Inviscid instability of compressible exponential boundary layer flows. *AIP Adv.* **11** (10), 105308.
- ZHAO, R., DONG, Y., ZHANG, X., WEN, C., LONG, T. & YUAN, W. 2021 Control of reflected waves with acoustic metasurfaces for hypersonic boundary-layer stabilization. *AIAA J.* **59** (6), 1893–1898.
- ZHAO, R., LIU, T., WEN, C.-Y., ZHU, J. & CHENG, L. 2019 Impedance-near-zero acoustic metasurface for hypersonic boundary-layer flow stabilization. *Phys. Rev. Appl.* **11** (4), 044015.
- ZHAO, R., WEN, C., ZHOU, Y., TU, G. & LEI, J. 2022 Review of acoustic metasurfaces for hypersonic boundary layer stabilization. *Prog. Aerosp. Sci.* **130** (100808), 100808.